Exchange fluxes between the Ría de Vigo and the shelf: A bidirectional flow forced by remote wind

Miguel Gilcoto,[1,2] Paula C. Pardo,[1] X. A. Álvarez-Salgado,[1] and Fiz F. Pérez[1]

Received 2 July 2005; revised 4 September 2006; accepted 6 November 2006; published 1 June 2007.

[1] In the Ría de Vigo (western coast of the Iberian Peninsula) the seasonal pattern associated with shelf winds at these latitudes produces upwelling/downwelling episodes that affect the residual circulation. The aim of this paper is to go deeply into the interaction between remote winds and the dynamics of the ria aided by an inverse model. In the Galician r ias the box models (inverse models) have been developed from a two-dimensional (2-D) point of view since the classical baroclinic residual circulation in positive estuaries has a vertical distribution (freshwater outflow through the surface layer and inflow through the bottom layer). However, recent work in the Ría de Vigo has shown the existence of a 3-D residual circulation in the seaward region of the ria. During upwelling (downwelling) conditions a coastal jet enters (leaves) the ria through the northern mouth and leaves (enters) through the southern mouth. The inverse model developed in this paper is a 3-D kinematic box model based on tracer and volume balances with the constraint of nonnegative vertical exchange coefficients. The fluxes obtained confirm, during some periods, the 3-D residual circulation overlying the classical 2-D scheme. It is shown how the 3-D pattern affects the inner ria, causing transversal differences in the flow field. In addition, the model results have been helpful in the discussion of a possible barotropic bidirectional flow associated with remote winds. The results have set the basis for the existence of a bidirectional flow originated by a barotropic interaction with the shelf upwelling.

Citation: Gilcoto, M., P. C. Pardo, X. A. Álvarez-Salgado, and F. F. Pérez (2007), Exchange fluxes between the Ría de Vigo and the shelf: A bidirectional flow forced by remote wind, *J. Geophys. Res.*, *112*, C06001, doi:10.1029/2005JC003140.

1. Introduction

[2] Subtidal exchange fluxes between shelves and estuaries, embayments or coastal seas are important processes directly related to the residual circulation of these marine systems. Residual circulation is a frequent matter of study [*Jay et al.*, 1997; *Uncles*, 2002] because it is the responsible for the import (export) of water, nutrients, contaminants, plankton, etc to (from) estuaries. Frequently, the key target of scientific studies deals with the forces driving the residual circulation [*Geyer et al.*, 2000; *Weisberg and Zheng*, 2003]. The identification of the driving force(s) is a cumbersome challenge because estuaries and shelves are regions where several physical processes (tides [*Álvarez Fanjul et al.*, 1997; *Inall et al.*, 2000; *Münchow et al.*, 1992], river discharge [*Csanady*, 1984; *Garvine*, 1987], winds [*Allen et al.*, 1983; *Allen and Smith*, 1981; *Torres et al.*, 2003], and several type of waves [*Allen*, 1975; *Jeans and Sherwin*, 2001], etc.) interact and manifest the general nonlinear nature of the sea dynamics. One should be aware of the transient nature of the sea dynamics in estuaries [*Jay and Flinchem*, 1997, 1999] because, at different time and spatial scales, the main processes driving the sea dynamics are different and they evolve and change in time and space. Thus it is also important to realize that the most frequent forcing in one estuary is not necessarily the most frequent in another estuary.

[3] The Ría de Vigo (Figure 1) is the southernmost of the Rías Baixas, four coastal embayments located in the western coast of the Iberian Peninsula, i.e., in the northern boundary of the NW Africa Coastal Upwelling System. At these latitudes (37°–43°N) shelf winds follow a seasonal pattern. Northerly winds favoring coastal upwelling are predominant from March–April to September–October, and southerly winds favoring coastal downwelling predominate the rest of the year [*Bakun and Nelson*, 1991; *McClain et al.*, 1986; *Wooster et al.*, 1976]. During upwelling episodes cold and nutrient rich Eastern North Atlantic Central Water (ENACW) [*Ríos et al.*, 1992b] is raised to the middle and inner shelf [*Álvarez-Salgado et al.*, 1993; *Fiúza*, 1983; *Fraga*, 1981] while the warm and salty surface waters of subtropical origin pile up in the shelf during downwelling episodes [*Frouin et al.*, 1990; *Haynes and Barton*, 1990, 1991]. Upwelling, downwelling, and the transitions among them are well-known short timescale events (2–4 days)

[1] Instituto de Investigaciones Marinas, Consejo Superior de Investigaciones Científicas, Vigo, Spain.
[2] Now at School of Chemistry, Physics, and Earth Sciences, Flinders University, Adelaide, South Australia, Australia.

0148-0227/07/2005JC003140

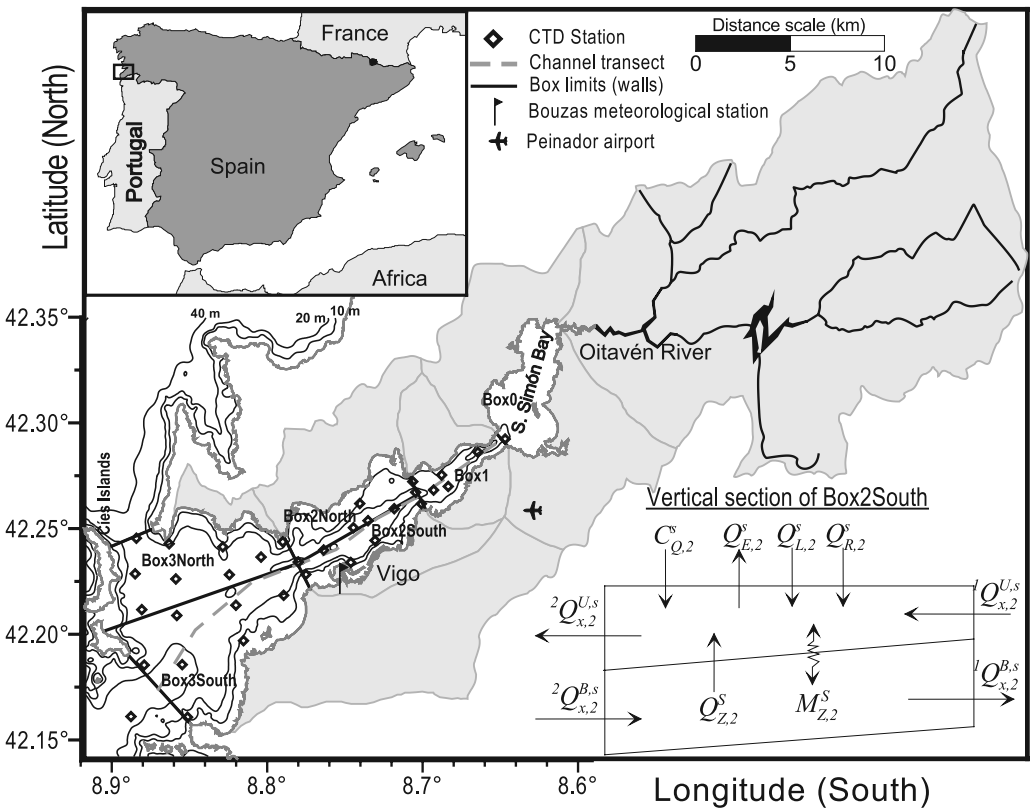

Figure 1. Chart of the Ría de Vigo. View of the four boxes. The CTD stations, the meteorological stations, the along-channel transect (dashed gray line), and the drainage basins for each semibox (shaded areas) are shown. A scheme of the vertical distributions of fluxes in the box 2 southern semibox is also depicted.

affecting the residual circulation of the Rias Baixas [*Álvarez-Salgado et al.*, 2000; *Gilcoto et al.*, 2001].

[4] *Souto et al.* [2003] have shown that the intrinsic 3-D nature of the coastal upwelling [*Smith*, 1983] interacts with the shallower northern (25 m) and deeper (50 m) southern mouths of the ria (Figure 1) generating a 3-D residual circulation in the inner ria. When an upwelling event occurs, the westward Ekman transport that conveys the surface water from the coast to the ocean is accompanied by an alongshore coastal jet that penetrates in the ria through the northern mouth, crosses the ria from north to south, and leaves the ria through the southern mouth. Under downwelling conditions the alongshore jet flows northward so it enters into the ria through the southern mouth and leaves the ria through the northern mouth.

[5] In addition to the 3-D residual circulation in the Ría de Vigo proposed by *Souto et al.* [2003], there is a comprehensive 2-D view of the residual circulation of the Galician rias in the literature. A simplified model of the reality in which the steady gravitational circulation with river flow origin and its induced two layer circulation scheme [*Hansen and Rattray*, 1965; *Officer*, 1976; *Pritchard*, 1956] was replaced by a two layer and non steady residual circulation significantly modulated by remote wind [*Álvarez-Salgado et al.*, 2000; *Fraga*, 1981; *Pardo et al.*, 2001; *Rosón et al.*, 1997]. This 2-D view has deeply influenced the evolution of the box models applied to the Galician rias, and, conversely, the box models have been a fundamental tool to analyze the importance of remote wind forcing in the rias [*Gilcoto et al.*, 2001].

[6] The influence that physical processes in the shelf have on estuaries [*Wong*, 2002], embayments [*Valle-Levinson et al.*, 2003] or ROFIs [*Simpson*, 1997] is nowadays a topic of active research [*Hickey and Banas*, 2003]. From a general point of view it is possible to summarize the studies on shelf-estuary interaction in two groups [*Valle-Levinson*, 1995]: (1) baroclinic interaction and (2) barotropic interaction. The first group is theoretically supported by the classical *Hansen and Rattray* [1965] gravitational theory of residual circulation, i.e., if the shelf processes change the density in the mouth of the estuary then the longitudinal density gradient will be increased (decreased) and, thus the gravitational circulation also will be intensified (decreased). Coastal upwelling/downwelling events [*Hickey et al.*, 2002; *Monteiro and Largier*, 1999] or river plumes from others estuaries [*Wong and Lu*, 1994; *Wong and Münchow*, 1995] can easily modify the density in the mouth of an estuary. The second group of papers (see *Valle-Levinson* [1995], *Janzen and Wong* [2002], and *Wong and Valle-Levinson* [2002] for an exhaustive list of such articles), which mainly deals with barotropic processes (tidal processes not included), are theoretically based in the analytical solutions of *Hansen and Rattray* [1965] and *Wang* [1979] for the momentum balance of an estuary under local winds (wind blowing

inside the estuary), and in the analysis developed by *Garvine* [1985] for estuaries under the influence of remote wind forcing.

[7] On the other hand, the arbitrary separation into baroclinic and barotropic as isolated processes is difficult and sometimes misleading. For example, it is possible to explain the coastal upwelling produced by the remote wind in barotropic terms [*Sverdrup*, 1938], and the interaction of the coastal upwelling with the estuary dynamics has been barotropically explained via sea level variations at the mouth of the estuary [*Garvine*, 1985; *Wang*, 1979]. However, it is clear that the freshwater outflow from the estuary to the shelf and the denser upwelled water change the baroclinic conditions in the shelf as well as the coastal upwelling process [*Charney*, 1955; *Yoshida*, 1955].

[8] Two main objectives are pursued in this manuscript. The first one is to develop, apply to a data set of field measurements, and discuss the results of a new inverse model (see *Wunsch* [1996] for an introduction of inverse models in oceanography) adapted to the 3-D nature of the residual circulation of the Ría de Vigo shown by *Souto et al.* [2003]. An inverse model that independently estimates the exchange fluxes in each mouth of the ria has never been done in previous box model applications to the Galician rias [*Gilcoto et al.*, 2001; *Míguez et al.*, 2001; *Pardo et al.*, 2001; *Prego and Fraga*, 1992; *Prego et al.*, 1990; *Rosón et al.*, 1997]. In order to obtain physically sound solutions, another requisite was imposed to the new inverse model: it must always return positive vertical exchange coefficients.

[9] The second aim of the paper is to discuss one of the current paradigms extensively claimed in articles of the formerly defined group ii): the association of bidirectional flow (two vertical layers flowing in opposite directions) with local wind forcing and the association of unidirectional flow (the whole water column flowing in the same direction) with remote wind forcing when the lateral depth variation of the estuary can be ignored [*Wong*, 2002]. Despite the V-shaped bathymetry of the Ría de Vigo, and the modifications that the bathymetry geometry may produce in the residual circulation [*Kasai et al.*, 2000; *Wong*, 1994], remote wind usually forces a bidirectional residual circulation.

2. Inverse Model

2.1. Box Model

[10] Four boxes were defined in the domain under study (Figure 1) limited horizontally by walls and vertically by surfaces. They were numbered from the head of the ria (the San Simón Bay labeled as box 0) to the seaward part of the ria (box 3). The most complex boxes are the seaward ones (box 2 and box 3) because each one is divided in four smaller semiboxes: vertically (upper and bottom semiboxes) separated by the surface defined by the level of no horizontal motion surface ($Z_C = Z_C(x, y, t)$) and horizontally (northern and southern semiboxes) separated by a wall along the longitudinal axis of the ria. Box 1 is only divided vertically (upper and bottom) by the Z_C surface. Finally, box 0 is wedge shaped; it has no semiboxes, and the wall common to box 1 is split in two vertical semiwalls (upper and bottom). Box 0 is wedge shaped because there is no wall at the head of the ria and only the river enters through this extreme of the model domain.

[11] The design of the boxes follows the recurrent two-layer box model applied to the Galician rias [*Álvarez-Salgado et al.*, 2000; *Gilcoto et al.*, 2001; *Pardo et al.*, 2001] but the horizontal split of the seaward boxes will allow us to calculate independent exchange fluxes in each mouth of the ria. In this sense the model will have an important 3-D nature. We also use the typical advection-mixing scheme included in box models of the Galician rias [*Míguez et al.*, 2001; *Rosón et al.*, 1997]: vertical (Q_Z) and horizontal (Q_x and Q_y) advection fluxes are considered but, since vertical gradients of tracers are one order of magnitude larger than horizontal gradients, only the vertical mixing/diffusion is considered through vertical exchange coefficients (M_Z). *Otto* [1975] showed that is possible to disregard the horizontal diffusion in the Rias Baixas because it is negligible in comparison with horizontal advection. In a 1-D box model the horizontal diffusion will not be negligible because there is a spatial (vertical) correlation between tracers and horizontal residual circulation: fresher water leaving the ria above the pycnocline and saltier water entering in the ria below the pycnocline. That is Z_C should be defined near the pycnocline, where the level of no movement of the bidirectional flow is supposed to be in order to reduce the spatial covariance.

[12] The vertical mixing/diffusion parameterization consists of a Fickian like expression ($-K_z \cdot A \cdot dC/dz$) with a mixing/diffusion coefficient (K_z) multiplied by the area (A) of the surface where it is applied and by the tracer gradient (dC/dz). Splitting the tracer gradient in a division of tracer and distance increments between boxes ($dC/dz \sim \Delta C/\Delta z$) it is possible to group all the terms except the tracer increment in an exchange coefficient ($M_Z = K_z \cdot A/\Delta z$). The exchange coefficient has units of cubic meters per second, the same units as a water flux. When multiplied by the tracer increment it accounts in a Fickian manner for all the purely diffusive transports of solutes plus for the mixing, dispersion, and advective transports at spatial scales smaller than the Z_C surface of the box. In fact, in the Ria de Vigo the subgrid advective transports of box models are responsible for most of the value of M_Z (tidal mixing, internal breaking waves, wind mixing, etc.).

[13] The physical insight of the exchange coefficient is that an equal volume of water per time (M_Z) is exchanged between the upper and bottom semiboxes [*Officer*, 1980; *Sakov and Parslow*, 2004]. That is, a parcel of water from the bottom semibox is entrained in the upper semibox and an equal volume of the upper semibox is incorporated into the bottom semibox. There is no net volume exchange between semiboxes but there is a net transport of tracer proportional to the difference of the average tracer concentration in the semiboxes. Although some authors have considered the exchange coefficient a "diffusive flux" [*Rosón et al.*, 1997], because it has units of a water flux and it mainly accounts for advective subgrid processes, it is not a water flux from the point of view of the box model because M_Z does not represent a net movement of water. Indeed, M_Z must be always positive to ensure that the mixing scheme works against tracer gradients, while a flux can be negative. There are rare and special conditions in which turbulent diffusion coefficients are negative [*Starr*,

1968] (namely, [*Holloway*, 1989; *Wunsch*, 1996, p. 297]) but the dimensions of the boxes and the temporal scale at which the model works preclude the existence of these conditions.

[14] Conservation of salt ($\upsilon = \rho \cdot S$), thermal energy ($\alpha = \rho \cdot C_p \cdot T$), mass and volume with nonsteady budget equations and the mixing scheme above are applied to the semiboxes. The corresponding budget equations for the semiboxes are set down in Appendix A with the corresponding notation explained in the notation section. Some points about the equations merit attention. The budgets are nonsteady but related to residual circulation, i.e., they are designed to work in subtidal frequencies and with variables averaged in space (boxes, walls, and surfaces) and time (tidal averages). Therefore, in the equations there are time derivatives of tracers approximated by time increments. In addition, there are terms accounting for the dynamic geometry of the boxes because we have chosen to include subtidal variations in $Z_C = Z_C(x, y, t)$ (the level of no motion) and in the sea level ($\eta = \eta(t)$). Then whereas the subtidal volume of a bottom semibox (V_B) is only affected by the movement of Z_C, the volume of the upper semibox (V_U) is also affected by the movement of η. The upper volume is estimated as

$$V_U = \breve{V}_U + A_{\text{sup}} \cdot \eta \tag{1}$$

$$\breve{V}_U = \overline{V} - V_B \tag{2}$$

where A_{sup} is the area of the sea level surface of the semibox (the area of the superior surface of the box, Z_C is the surface in the middle of the box and the bathymetry that on the bottom), η is assumed to be spatially homogeneous (the subtidal sea level is considered flat all over the ria), and $\overline{V}$ is the mean sea level volume of the box (upper plus bottom semiboxes). On the other hand, the subtidal movement of Z_C is not a movement of the fluid because Z_C is not defined by fluid particles but by the points where the horizontal velocity is null. So the vertical advective flux estimated with the model (Q_Z) must be corrected with the virtual vertical flux associated with the arbitrary movement of Z_C ($Q_Z^{Z_C}$) to obtain the real vertical flux of the fluid (Q_Z^f)

$$Q_Z^f = Q_Z - Q_Z^{Z_C} \tag{3}$$

$$Q_Z^{Z_C} = \frac{\Delta \breve{V}_U}{\Delta t} = -\frac{\Delta V_B}{\Delta t} \tag{4}$$

2.2. Inverse Method

[15] The total number of semiboxes in the model is eleven: four in both boxes 3 and 2, two in box 1, and one in box 0. Since we apply four budget equations (volume, mass, salt, and thermal energy) to each semibox there are a total of 44 budget equations. The incognita are: sixteen horizontal advective fluxes (Q_x) in the walls separating boxes, four horizontal advective fluxes (Q_y) in the walls along the longitudinal axis of the ria defining the northern and southern semiboxes of boxes 2 and 3, and five vertical advective fluxes (Q_Z) and exchange coefficients (M_Z) in all the boxes (except box 0). Summing up, we have a system of 44 equations with 30 unknowns, i.e., an overdetermined system of equations. However, the effective rank of the coefficient matrix will be less than 44 because there would be correlations between the mass conservation and the rest of the conservation equations. In the worse case the effective rank will be 33 (33 independently equations and 30 unknowns).

[16] The strategy adopted was not to solve the whole system of equations in one step but solving it box after box starting from box 0. Then, the resulting horizontal fluxes in common with box 1 are used as boundary conditions for solving the system of equations of box 1 in the next step and so on. With this strategy we solve four overdetermined systems of equations: the 4×2 (equations times unknowns) of box 0, the 8×4 of box 1, and the 8×16 of boxes 2 and 3. Two reasons justify this strategy. First, though more steps are involved with this solving process it is better when looking for outliers that can reveal potential errors both in the source code of the algorithms and in the source data set. Second, if all the boxes are solved in one step the results would be very influenced by the seaward boxes because their equations will have coefficients larger than the internal ones (a simple effect of box dimensions). With this strategy, the first two boxes do not depend on the equations of the seaward boxes. Normally these inner boxes present the larger vertical gradients (two or three times larger) and *Gilcoto et al.* [2001] have shown that the errors of the horizontal advective fluxes estimated with a box model are inversely proportional to the vertical gradients of tracers. *Gilcoto et al.* [2001] derived an analytical solution to calculate the horizontal fluxes in a wedge shape box and then they were able to analyze the analytical error of the solution.

[17] The equations set forth in Appendix A are concise and explicit but the indices complicates them. It is better to represent any one of the four systems (one for each box), with a general matrix expression

$$\mathbf{A} \cdot \mathbf{x} = \mathbf{y} \tag{5}$$

where the column vector $\mathbf{x}$ ($n \times 1$) is filled with the unknowns of each box (fluxes in the left hand side of the equations in Appendix A), the matrix $\mathbf{A}$ ($m \times n$) with the coefficients of the unknowns, and the column vector $\mathbf{y}$ ($m \times 1$) with the terms in the right hand side of the equations (horizontal fluxes estimated in the previous box, sources and sinks of property and time derivatives). Because the system of equations of the four boxes is overdetermined, a Weighted Minimum Least Squares approximation is suitable to find an optimum solution [*Gay et al.*, 2004; *Gilcoto et al.*, 2001]. In addition, we are also seeking for solutions fulfilling the positive vertical exchange coefficient condition. Thus the problem is to find a set of fluxes, exchange coefficients being positive, that minimizes the weighted sum of squared residuals. Mathematically,

$$Min\left\{(\mathbf{A} \cdot \mathbf{x} - \mathbf{y})^T \cdot \mathbf{W}^{-1} \cdot (\mathbf{A} \cdot \mathbf{x} - \mathbf{y})\right\} \quad \text{subject to } M_Z \geq 0 \tag{6}$$

where $\mathbf{W}$ (m × m) is a diagonal matrix with the diagonal elements being the square of the norm of the corresponding row of the augmented matrix [$\mathbf{A}|\mathbf{y}$]. Thus $\mathbf{W}$ weights the relative magnitudes of the residuals ($\mathbf{y} - \mathbf{A} \cdot \mathbf{x}$) and produces adimensional budget equations. The $\mathbf{W}$ elements for the equations of volume conservation were multiplied by 10^{-3} in order to force the conservation of volume (the residuals of the volume conservation equations will be very low) because the box models applied to the Galican rias have performed quite well with this constraint [*Gilcoto et al.*, 2001; *Pardo et al.*, 2001; *Rosón et al.*, 1997]. It is clear that, at our timescales, the rias are neither increasing nor decreasing their mean sea level.

[18] The diagonal disposition of the $\mathbf{W}$ elements allows us to rewrite it as $\mathbf{W}^{-1} = \mathbf{w} \cdot \mathbf{w}^{\mathrm{T}}$ where $\mathbf{w}$ (m × m) is also diagonal and its elements are the inverse of the root square of the corresponding elements of $\mathbf{W}$. So, we can obtain the more general expression

$$Min\left\{(\mathbf{E}\cdot\mathbf{x}-\mathbf{f})^{T}\cdot(\mathbf{E}\cdot\mathbf{x}-\mathbf{f})\right\} \quad \text{subject to } \mathbf{G}\cdot\mathbf{x}\geq\mathbf{h} \tag{7}$$

with $\mathbf{E} = \mathbf{w}^{\mathrm{T}} \cdot \mathbf{A}$, $\mathbf{f} = \mathbf{w}^{\mathrm{T}} \cdot \mathbf{y}$, the matrix $\mathbf{G}$ compiles the coefficients for the constraints (one row per constraint, in our case one row per M_Z having all the elements zeros except an one in the column corresponding with the M_Z index in $\mathbf{x}$), and $\mathbf{h}$ is a column vector in which each row contains the right-hand side value of each constraint (in our case is a vector with zeros).

[19] The mathematical problem (7) has been numerically solved with the linear least squares with linear inequality constraints (LSI) algorithm developed by *Lawson and Hanson* [1995, chapter 23]. The LSI problem is subject to the Kuhn-Tucker theorem [see *Lawson and Hanson*, 1995, p. 159; see *Wunsch*, 1996, p. 299] and only will find an optimum solution $\hat{\mathbf{x}}$ if E is full rank and the constraints are consistent (i.e., they are compatible and guarantee a feasible solution). The Lawson and Hanson LSI algorithm is based on their nonnegative least squares (NNLS) algorithm [*Lawson and Hanson*, 1995; *Mackas et al.*, 1987; *Wunsch*, 1996, section 5.1] and on the single-value decomposition (SVD) [*Golub and Loan*, 1996; *Lawson and Hanson*, 1995; *Wunsch*, 1996]. Since the latter two algorithms (NNLS and SVD) are well known and already implemented in commercial software (Matlab from Mathworks, for example), some brief indications to implement the LSI with NNLS and SVD are presented in Appendix B.

2.3. Robustness of the Inverse Method

[20] We are facing two problems to evaluate the robustness of the optimum solutions ($\hat{\mathbf{x}}$) found with the LSI algorithm. In fact, both problems have the same nature: they are nonlinear. First, the inequalities included in the inverse model make nonlinear the propagation of the error through the systems of equations (6) and (7). Second, the standard linear expressions to estimate the uncertainty (variance) of the solution of least squares problems [*Wunsch*, 1996, chapter 3] do not account for the errors in the matrix of coefficients ($\mathbf{A}$ in equation (6)). Considering the errors in $\mathbf{A}$, as we want, the problem becomes nonlinear [see *Wunsch*, 1996, chapter 5].

[21] Although the total inversion (TI) algorithm of *Tarantola and Valette* [1982] solves the second source of nonlinear behavior it does not support inequalities. Thus the first source of nonlinearities had excluded the use of the TI algorithm. To overcome the nonlinearities in the error calculation we have used a perturbation method as *Maamaatuaiahutapu et al.* [1998] and *Gilcoto et al.* [2001] have done in water mass analysis and box models, respectively.

[22] After an appropriate error bounds (standard deviation) for each of the elements of $\mathbf{A}$ and $\mathbf{y}$ matrices ($\sigma_{A_{i,j}}$ and $\sigma_{y_{i,1}}$ respectively) has been selected, 10,000 perturbed $p\mathbf{A}$ and $p\mathbf{y}$ matrices have been produced following normal distributions with $\sigma_{A_{i,j}}$ and $\sigma_{y_{i,1}}$ standard deviations and with $A_{i,j}$ and $y_{i,1}$ means. Then 10,000 perturbed matrix weights ($p\mathbf{W}$) have been obtained and the corresponding 10,000 LSI systems have been set:

$$Min\left\{(p\mathbf{E}\cdot\mathbf{x}-p\mathbf{f})^{T}(p\mathbf{E}\cdot\mathbf{x}-p\mathbf{f})\right\} \quad \text{subject to } \mathbf{G}\cdot\mathbf{x}\geq\mathbf{h} \tag{8}$$

which have given us a total of 10,000 perturbed solutions $p\mathbf{x}$. We have estimated the uncertainty of our optimum solution ($\boldsymbol{\sigma}_{\hat{\mathbf{x}}}$) as the standard deviation of the 10,000 perturbed solutions

$$\boldsymbol{\sigma}^2_{\hat{\mathbf{x}}} = \frac{\sum_{i=1}^{10000}(p\mathbf{x}_i - \hat{\mathbf{x}})^2}{10000} \tag{9}$$

being $\hat{\mathbf{x}}$ the optimum solution to (7).

[23] The selected values, standard deviations, for the rows in $\boldsymbol{\sigma}_{\mathbf{A}}$ accounting for the salt content, thermal energy and density perturbations are explained in section 3.1 because they depend on the temporal and spatial averages in the walls and surfaces of the boxes. The elements of $\boldsymbol{\sigma}_{\mathbf{A}}$ accounting for the volume perturbations are simply set to zero because we are working under the assumption of strict volume conservation.

[24] The structure of the elements of the $p\mathbf{y}$ matrix is organized with thee types of terms: the perturbed temporal derivatives (a terms), the perturbed sources and sinks of tracers (b terms), and the perturbed fluxes coming from the previous box (c terms). Each term is perturbed with its own standard deviation and, then, they are summed up. We do not perturb each element of $\mathbf{y}$ with a corresponding $\boldsymbol{\sigma}_{\mathbf{y_{i,1}}}$ as a whole:

$$p\mathrm{y}_{\mathrm{i,1}} = \left(p\mathrm{y}_{\mathrm{i,1}}\right)_a + \left(p\mathrm{y}_{\mathrm{i,1}}\right)_b + \left(p\mathrm{y}_{\mathrm{i,1}}\right)_c \tag{10}$$

The c terms are obtained directly from the perturbed solution of the previous box. The b terms are calculated with an estimated standard deviation equal to a 15% of the source and sink values (section 3.2). Furthermore, the standard deviations to estimate the a terms are a function of the standard deviations of the volume mean values of the tracers in the semiboxes:

$$\sigma^2_{\left(y_{i,1}\right)_a} = \sigma^2\left(\frac{\Delta V\cdot Var_i}{\Delta t}\right) \approx \sigma^2\left(\frac{(V\cdot Var_i)_{t=2}-(V\cdot Var_i)_{t=1}}{\Delta t}\right) = \sigma^2_{Var_i}\cdot\left(\frac{V^2_{t=1}+V^2_{t=2}}{(\Delta t)^2}\right) \tag{11}$$

where we have applied the error propagation formula [*Bevington and Robinson*, 1992]; Var_i is the volume average in the semibox of the thermal energy, density or salt content as indicated by the i index; V is the volume of the semibox; and we have assumed that the variance of the tracer is the same at times $t = 1$ and $t = 2$. The values given to the different $\sigma^2_{Var_i}$ are explained in the section 3.1 together with those conforming the $\boldsymbol{\sigma}_{\mathbf{A}}$ matrix.

3. Data Set

3.1. Thermohaline Data

[25] The application of the box model to estimate exchange fluxes between the ria and the shelf requires an ample and varied data set. In 1997, on board the R/V *Mytilus,* a total of 26 CTD (conductivity-temperature-depth) surveys were conducted in the Ría de Vigo. The surveys were distributed in five different campaigns: (1) a spring campaign with six surveys on 7, 10, 14, 17, 21, and 23 April; (2) an early summer campaign with six surveys on 1, 4, 8, 11, 15, and 18 July; (3) a summer-autumn campaign with six surveys on 15, 18, 22, 25, 29 September and 2 October; (4) an autumn campaign with four surveys on 28 and 31 October and 4 and 6 November; and (5) a late autumn campaign with four surveys on 1, 5, 8, and 11 December. A total of 34 CTD stations (Figure 1) were occupied with a SeaBird SBE-25 CTD in each survey. The temperature and salinity fields were sampled with the instrumental resolution indicated in the calibration sheets of the SBE-25 probe (σ_T = 0.005°C, σ_S = 0.005, and σ_P = 0.01 dbar for temperature, salinity, and pressure, respectively). The related resolutions of the derived magnitudes were estimated with

$$\begin{aligned}
\sigma_\rho &\approx \sqrt{\sigma_T^2 \cdot \left(\frac{\partial \rho}{\partial T}\right) + \sigma_S^2 \cdot \left(\frac{\partial \rho}{\partial S}\right) + \sigma_P^2 \cdot \left(\frac{\partial \rho}{\partial P}\right)} \approx 0.004 \text{ kg m}^{-3} \\
\sigma_\upsilon &\approx \sqrt{\sigma_S^2 \cdot \rho^2 + \sigma_\rho^2 \cdot S^2} \approx 5 \text{ m}^{-3} \\
\sigma_\alpha &\approx C_P \sqrt{\sigma_\rho^2 \cdot T^2 + \sigma_T^2 \cdot \rho^2} \approx 20000 \text{ J m}^{-3}
\end{aligned} \tag{12}$$

for density (σ_ρ), salt content (σ_υ), and thermal energy (σ_α), respectively, in the temperature, salinity, and pressure range of the data set.

[26] The stations were distributed all over the ria with the maximum spatial density possible in 6–7 hours of vessel work. The Ría de Vigo has a semidiurnal tidal regime with a tidal range of 2 m in neap tides and 4 m in spring tides and a tidal excursion of 2.5–3 km. In order to reduce spatial tidal aliasing in the recorded data we tried to sample the maximum number of stations in a tidal semiperiod (~6 hours) and the surveys were always conducted against the tidal current, i.e., when the situation was of high tide the surveys started in the seaward stations and in low tide the surveys started in the innermost stations. After the raw CTD data were processed, filtered, and purged with the standard prescriptions of the CTD manufacturer [*Sea-Bird Electronics Inc.*, 2000, 2003] the data were used to build up 3-D grids of temperature and salinity. The 3-D grids were calculated with an inverse distance 3-D interpolation in a metric system of reference: the UTM (universal transversal Mercator) coordinates of the stations (x, y) and the depth (z) of each CTD sample. The value of a variable (Var = temperature or salinity) in a node (n) of a survey grid is the distance weighted average of all the CTD samples (r) in the survey:

$$Var_n = \frac{\sum_r d_r \cdot Var_r}{\sum_r d_r} \tag{13}$$

where the weights (d_r) depend on the inverse distance between the sample and the node:

$$\begin{aligned}
d_r^x &= ((x_r \cdot \cos\phi + y_r \cdot \sin\phi) - (x_n \cdot \cos\phi + y_n \cdot \sin\phi))^2 \\
d_r^y &= ((y_r \cdot \cos\phi - x_r \cdot \sin\phi) - (y_n \cdot \cos\phi - x_n \cdot \sin\phi))^2 \\
d_r^z &= (z_r - z_n)^2 \\
d_r &= \left(f_x^2 \cdot d_r^x + f_y^2 \cdot d_r^y + f_z^2 \cdot d_r^z\right)^{-e/2}
\end{aligned} \tag{14}$$

and the set of parameters selected to adjust the weighting distances is

$$\begin{aligned}
f_x &= 1 \quad & f_y &= 1.5 \quad & f_z &= 2000 \\
e &= 0.5 \quad & \phi &= 30^\circ
\end{aligned} \tag{15}$$

The f factors which control the relative scales among the geographic coordinates and their values were chosen because the seaward basin of the ria is 1.5 times narrower than longer and its longitude is approximately 2000 times its depth. The rotation angle (ϕ) matches the angle between the UTM X axis and the longitudinal axis of the ria. Finally, the exponent e was arbitrarily chosen as a function of a subjective evaluation of the interpolation results. The exponent, that we selected 0.5, results in smoothing the results. A higher exponent would produce eye structures close to each CTD station and a lower one would spatially homogenize the fields. Once the 3-D interpolated grids of temperature and salinity were calculated the derived 3-D grids of density, salt content, and thermal energy were obtained with the corresponding algorithms and formulas (notation section).

[27] The objective of the interpolation was to obtain thermohaline fields closer to the tidal average. There is only one CTD profile per station and survey, so the interpolation acts as a spatial filter "mixing" the samples of different stations like the tide will do with a profile sampled several times during a tidal period in a station. With the 3-D interpolated grids the spatial (walls, volumes and surfaces) averaged thermohaline values needed to fill the matrix of coefficients ($\mathbf{A}$) and the matrix of constants ($\mathbf{y}$) of the inverse model were calculated.

[28] The calculation of spatial averages depends on the definition of Z_C (semibox dynamic geometry). For each survey, the Z_C surface was obtained from the density field calculated with the temperature and salinity 3-D interpolated grids. The level of no motion in the Galician rias has been associated with the gravitational circulation and it was determined with the depth of the mean vertical density (or salinity) or with the depth of the pycnocline (or halocline) [*Pardo et al.*, 2001; *Rosón et al.*, 1997]. However, as the main forcing of the two-layer residual circulation is coastal upwelling (see section 4.2.2) an estimation of Z_C more independent of bathymetry has been chosen. To calculate

$Z_C(x_n, y_n)$ in each horizontal grid node, we defined vertical sections perpendicular to the main axis of the ria and 200 m thick. Then, the average density of each section was obtained. $Z_C(x_n, y_n, t)$ is the depth at which the section mean density is found in each horizontal grid node.

[29] The variance associated to a interpolated value in a node is calculated with the error propagation formula [*Bevington and Robinson*, 1992], that is

$$\sigma^2_{Var_n} = \sum_r \sigma^2_{Var_r} \cdot \left(\frac{\partial Var_n}{\partial Var_r}\right)^2 = \sigma^2_{Var} \cdot \sum_r a_r^2 \le \sigma^2_{Var}$$
$$\text{with } a_r = \frac{d_r}{\sum_r d_r} \text{ and } \sigma^2_{Var_r} = \sigma^2_{Var} \tag{16}$$

and since the a factors calculated in the interpolation are $a_r < 1$ the sum of their squares is also lower than (or nearly equal) to 1. This means that the interpolation reduces slightly the standard deviation of the temperature and salinity values originality measured with the CTD. Anyway, the reduction is small and we have kept the former standard deviations of the interpolated variables ($\sigma_T = 0.005$°C and $\sigma_S = 0.005$) and those of the derived variables ($\sigma_\rho = 0.004$ kg m^{-3}, $\sigma_\upsilon =$ 5 m^{-3}, and $\sigma_\alpha = 20000$ J m^{-3}).

[30] The 3-D inverse distance interpolation produces in the interpolated nodes a direct reduction in the variance of the original measured tracers that, finally, we have not taken into account. The interpolation also produces an indirect and very important reduction in the variance of the volume and surface averaged tracer values ($\langle Var_i \rangle$). The reduction is proportional to the square of the number of nodes averaged:

$$\langle Var_i \rangle = \frac{\sum_n^M Var_{i,n}}{M}$$
$$\sigma^2_{\langle Var_i \rangle} = \frac{\sum_n^M \sigma^2_{Var_{i,n}}}{M^2} = \frac{\sigma^2_{Var_i}}{M} \tag{17}$$

since all the nodes are subject to same variance for each tracer. The interpolation generates a great number of nodes and this allows us to reduce the variance. This means that, for example, the standard deviation of a volume averaged tracer (equation (17)) is at least 158 times lower than the standard deviation of a node (equation (16)) because the smallest semibox has more than 25,000 interpolated nodes in its interior.

[31] Therefore we could apply an important reduction (at least two orders of magnitude) to the standard deviations of the tracer averaged values used to perturb the LSI system of equations (equation (8)) and conforming the matrices $\boldsymbol{\sigma}_\mathbf{A}$ and $\sigma_{(\mathbf{y})_a}$ of section 2.3. However, we have maintained the values $\sigma_\rho = 0.004$ kg m^{-3}, $\sigma_\upsilon = 5$ m^{-3}, and $\sigma_\alpha = 20{,}000$ J m^{-3} to perturb the LSI system of equations, i.e., we have greatly relaxed the limits of the perturbations in order to do a more robust estimate of the error of the inverse model solution.

3.2. Parameterization of Source and Sink Terms With Meteorological Data

[32] In addition to the CTD data, meteorological variables (Figure 2) were recorded at three different stations (Figure 1). In the INM (Spanish National Meteorological Institute) meteorological station at Bouzas, the local wind (Figure 2a; W_p is the component parallel to the main axis of the ria, southwesterly winds are positive, and W_t is the transversal component, southeasterly winds are positive), the relative humidity (H in percent), the air temperature (T_{air} in °C) (Figure 2b), and the direct precipitation over the ria (L in mm d^{-1}) (Figure 2c) were recorded. The INM meteorological station of the Peinador Airport supplied us the cloudiness (N in octas, not shown) and the rainfall (not shown though it is very similar to that of Bouzas, Figure 2c).

[33] The complete meteorological data set allow us to estimate the source and sink terms that appear in the budget equations of the box model (Appendix A). The normalized continental runoff (q_R, m^3 s^{-1} per m^2 of drainage basin, Figure 2c) for the drainage basin of the Oitavén River (346.9 km^2, Figure 1) was estimated with the rainfall of Peinador ($L_n^{Peinador}$, mm d^{-1} with n running from the previous day, $n = 1$, to one year before, $n = 365$) following the algorithm of *Ríos et al.* [1992a]:

$$q_R = 10^{-6} \cdot \left(0.007538 + 0.007889 \cdot \frac{0.25}{0.75 - (0.75)^{366}} \cdot \sum_{n=1}^{365} L_n^{Peinador} \cdot (0.75)^n\right) \tag{18}$$

and the final continental runoff (Q_R) for each drainage basin (Figure 1) of area A_R discharging in the corresponding semibox (j = 0 ... 3 the box index, i = n,s the northern-southern semibox index) is

$$Q^i_{R,j} = q_R \cdot A^i_{R,j} \tag{19}$$

[34] The direct rainfall water flux (Q_L) was estimated with the precipitation data in Bouzas:

$$Q^i_{L,j} = \frac{A^i_{\text{sup},j} \cdot L}{864 \cdot 10^5} \tag{20}$$

[35] The evaporation flux (Q_E), positive when evaporation occurs and negative if condensation, was parameterized with

$$Q^i_{E,j} = \frac{A^i_{\text{sup},j} \cdot e^i_j}{864 \cdot 10^5} \tag{21}$$

with e (mm d^{-1}) the evaporation rate in the northern ($i = n$) or southern ($i = s$) surface of the box j estimated with the equation given by seminal work of *Otto* [1975]

$$e^i_j = (0.26 + 0.077 * W) \cdot \left(e_{sal}\left(T^i_{\text{sup},j}, T_{air}, S^i_{\text{sup},j}\right) - e_{wair}\left(T^i_{\text{sup},j}, T_{air}\right) \cdot \frac{H}{100}\right) \tag{22}$$

where W, T_{air} and H are, respectively, the wind celerity (m s^{-1}), air temperature (°C) and relative humidity (%). The evaporation rate is based on the pure water vapor pressure equation (e_w, equation (23)) at temperature T (°C)

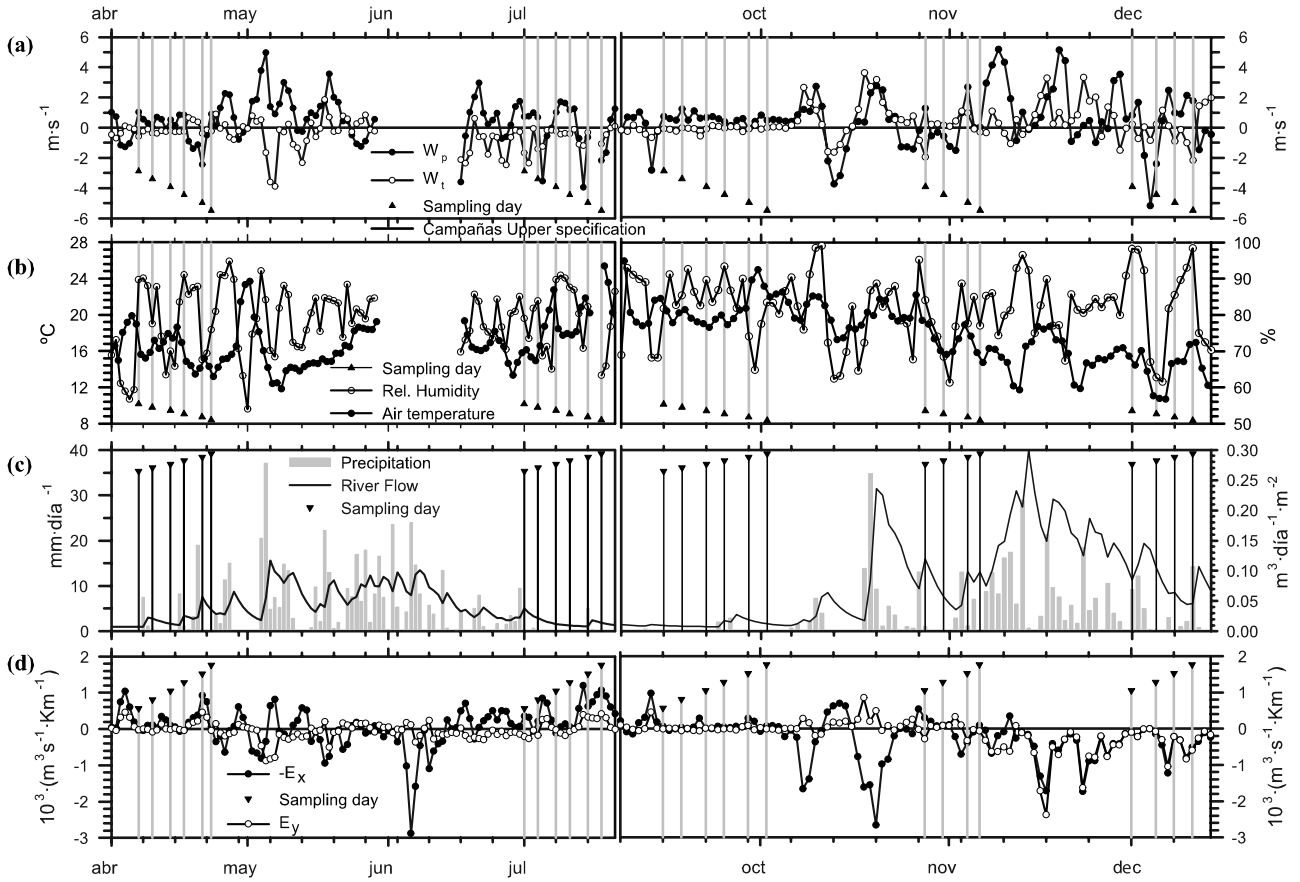

Figure 2. Time series of atmospheric data with the CTD surveys signaled by triangles. (a) Component parallel to the main axis of the ria (W_p, solid circles, southwesterly winds are positive) and the transversal component (W_t, open circles, southeasterly winds are positive) of local wind. (b) Air temperature (°C, solid circles, left scale) and the relative humidity (%, open circles, right scale) at the Bouzas meteorological station. (c) Precipitation in Bouzas (mm d^{-1}, line, left scale) and the normalized river discharge (m^3 d^{-1} m^{-2}, shaded histogram, right scale). (d) Negative of the offshore Ekman transport ($-E_x$, solid circles) and the alongshore Ekman transport (E_y, open circles).

parameterized with a sixth-order polynomial fit to the data shown in Table D109 of *Weast* [1969]. However, it has to be corrected by means of equations (24) and (25) because of the salinity (e_{sal} [*Sverdrup et al.*, 1942, p. 115]) and the presence of air (e_{wair} [*Gill*, 1982, Appendix A4.2]) respectively.

$$e_w(T) = 6.1117675 + 0.443986062 \cdot T + 0.0143053301 \cdot T^2 + 2.6502724210^{-4} \cdot T^3 + 3.02246994 \cdot 10^{-6} \cdot T^4 + 2.03886313 \cdot 10^{-8} \cdot T^5 + 6.38780966 \cdot 10^{-11} \cdot T^6 \quad (23)$$

$$e_{sal}(T_{water}, T_{air}, S) = e_{wair}(T_{water}, T_{air}) \cdot (1 - 0.000537 \cdot S) \quad (24)$$

$$e_{wair}(T_{water}, T_{air}) = e_w(T_{water}) \cdot \left(1 + 1.01325 \cdot 10^{-3} \cdot \left(4.5 + 0.0006 \cdot T_{air}^2\right)\right) \quad (25)$$

[36] Only one source/sink term appearing in Appendix A remains unexplained, the net radiative energy exchange between the sea and the atmosphere (C_Q, J s^{-1}). It is the sum of four individual processes [*Gill*, 1982] that, in fact, include radiative and nonradiative processes:

$$C_Q = C_{Q_E} + C_{Q_{SW}^{rad}} + C_{Q_{LW}^{rad}} + C_{Q_{sen}} \quad (26)$$

[37] The radiative processes are the direct short wave solar irradiation ($C_{Q_{SW}^{rad}}$) and the net long wave (or back radiation) earth-atmosphere radiation ($C_{Q_{LW}^{rad}}$). While the nonradiative terms are the air-sea exchange (sensible heat or direct thermal transfer, heat conduction, $C_{Q_{sen}}$) and the latent heat loss by evaporation (C_{Q_E}). The four terms were calculated with bulk formulae.

[38] The parameterization for the latent heat loss is:

$$C_{Q_{E,j}}^i = -Q_{E,j}^i \cdot \left(\alpha_{\mathrm{sup},j}^i + 2456.008 \cdot 10^6\right) \quad (27)$$

the short wave solar irradiation is a modification of the *Mosby* [1936] formula

$$C^i_{Q^{rad}_{SW},j} = 0.94 \cdot A^i_{\mathrm{sup},j} \cdot \left[213.7 + 777.2 \cdot \sin^2\left(\pi \cdot \frac{(355-n)}{365}\right)\right] \cdot (50.417 - 4.474 \cdot N) \cdot \frac{4.184}{600} \quad (28)$$

with N being the cloudiness (octas) recorded in Peinador and n the Julian date. The net long wave radiation was obtained with the bulk formula given by *Pickard and Emery* [1990]

$$C^i_{Q^{rad}_{LW},j} = -A^i_{\mathrm{sup},j} \cdot \left(143 - 0.9 \cdot T^i_{\mathrm{sup},j} - 0.46 \cdot H\right) \cdot (1 - 0.1 \cdot N) \quad (29)$$

and finally, the sensible heat exchange was inferred with the parameterization of *Otto* [1975] for the nearby Ría de Arousa:

$$C^i_{Q_{sen},j} = -24.88 \cdot (0.38 + 0.114 \cdot W) \cdot \left(T^i_{\mathrm{sup},j} - T_{air}\right) \cdot A^i_{\mathrm{sup},j} \cdot \frac{4184}{8640} \quad (30)$$

3.3. Ekman Transports in the Continental Shelf

[39] The third meteorological station was an Aanderaa portable station installed by the IEO (Spanish Institute of Oceanography) in the nearby Ons Island (42.35°N, not shown in Figure 1, located 15 km northward of Cíes Islands) during the FEUGA project with the aim of recording the shelf winds ($\vec{W} = W_x \cdot \hat{i} + W_y \cdot \hat{j}$). Using the remote wind and the parameterizations of *Bakun* [1973] (the wind drag coefficient C_d = 0.0014, the air density ρ_{a_3} = 1.22 kg m^{-3}, the seawater density ρ = 1025 kg m^{-3}, and the Coriolis factor f) the Ekman transports (E_x and E_y, m^3 s^{-1} per km of coast, equation (31)) were estimated (Figure 2d). Considering the orientation of the west coast of Galicia and with the Ekman transports referred to the classical oceanographic system of reference, negative E_x will induce upwelling in the ria and conversely positive E_x will generate downwelling conditions.

$$E_x = \frac{C_d \cdot \rho_a}{\rho \cdot f} \cdot W \cdot W_y \qquad E_y = -\frac{C_d \cdot \rho_a}{\rho \cdot f} \cdot W \cdot W_x \quad (31)$$

3.4. Sea Level Data

[40] The last time series needed to run of the inverse model were the sea level measurements. We have used the sea level data recorded by the tidal gauge of Puertos del Estado (http://www.puertos.es) in the Harbor of Vigo. The sea level time series was filtered with a $A^2_{24}A_{25}$ Godin filter [*Godin*, 1972] in order to obtain the subtidal sea level values used in the budget equations (Appendix A).

4. Results and Discussion

4.1. Inverse Model Results

[41] The matrix of coefficients (**A**) in equation (5), that is applied to each box defined in the ria, contains elements resulting from the time average of two consecutive CTD surveys. These elements are mean values of the spatial averaged tracer values in semiwalls, semiboxes, and semisurfaces obtained in two consecutive CTD surveys. On the other hand, the time derivatives in matrix **y** are estimated with the volume averaged tracer values difference of two consecutive CTD surveys divided by the time interval between them. Thus the box model estimates the advective and nonadvective time and spatial average fluxes between two consecutive CTD surveys. We are calculating the mean fluxes that drive the tracer fields from their distribution in a given survey to their distribution in the next survey. This means that the first three campaigns give us five box model results each one (six surveys each) and the last two campaigns only three results (four surveys each), producing a total of 21 exchange flux estimations. It is a cumbersome task trying to graphically show all the box model results (21 sets of 24 fluxes). To analyze the residual circulation in the middle and seaward zones of the ria (section 4.2) the estimated fluxes of box 3 are listed in Table 1. In addition two interesting, clear, and contrasting events of remote wind forcing residual circulation recorded during the CTD campaigns have been selected to graphically portray the box model results.

4.1.1. Upwelling Event

[42] During the early summer CTD campaign the Ekman transport perpendicular to the western Galician coast (E_x) was mainly upwelling favorable (Figure 2d) and the continental runoff was low (Figure 2c) because of the dry season: low precipitation (Figure 2c) and daily average air temperature between 16° and 24°C (Figure 2b). The three last surveys of the campaign were surveyed during an intense upwelling event (Figure 2d). The effects of the upwelling in the temperature and salinity fields of the ria are shown in Figure 3 through contours of horizontal distributions in the surface (Figures 3a–3f) and vertical sections (Figures 3g–3l) along the main channel (dashed gray line in Figure 1). The distributions have been calculated with the 3-D interpolated CTD data for each survey.

[43] On 11 July, 1 day before the beginning of the upwelling event and 6 days after a less intense upwelling event (Figure 2d), the ria presented marked vertical temperature gradient (Figure 3j). The residual circulation in these transitional days between upwelling events was slow (Ekman transport low) and air temperature relatively high (Figure 2b). The surface ria was heated and the sea surface temperature ranged between 19.5°C in the boundary with San Simón Bay and 17.4°C in the southern mouth (Figure 3d). The cold water (below 13.5°C), introduced in the deeper zones of the ria by the previous upwelling event, increased the vertical temperature gradient (Figure 3j). The vertical distribution of salinity on 11 July (Figure 3g) also shows the saltier (>35.8) shelf water inside the ria and the surface salinity distribution (Figure 3a) depicts isohalines perpendicular to the main axis of the ria. On 12 July the upwelling event started to act on the residual circulation of the ria and modified the thermohaline fields. In the vertical sections of the next two surveys (Figures 3h, 3i, 3k, and 3l) it is shown how the coldest (<13.5°C) and saltier (>35.7) shelf water progressively occupied more volume in the deeper seaward zones of the ria and penetrated into the shallower inner zones, increasing the average salinity, decreasing the

Table 1. Advective Fluxes and Corresponding Errors Estimated With the Inverse Model Applied to Boxes 2 and 3[a]

Start	End	${}^{2}Q^{U,s}_{x,3}$	${}^{2}Q^{B,s}_{x,3}$	${}^{2}Q^{U,n}_{x,3}$	${}^{2}Q^{B,n}_{x,3}$	${}^{1}Q^{U,n}_{x,3}$	${}^{1}Q^{B,n}_{x,3}$	${}^{1}Q^{U,s}_{x,3}$	${}^{1}Q^{B,s}_{x,3}$
7-4[b]	10-4	6503 ± 390	−509 ± 260	−1628 ± 385	−4419 ± 290	−20 ± 8	−810 ± 75	437 ± 7	370 ± 74
10-4	14-4	−786 ± 3	1099 ± 16	−450 ± 2	142 ± 19	−616 ± 2	413 ± 5	−392 ± 2	592 ± 5
14-4[c]	17-4	384 ± 3	1107 ± 30	−99 ± 4	−1374 ± 34	39 ± 0	−17 ± 4	65 ± 0	−84 ± 4
17-4	21-4	462 ± 3	655 ± 54	−203 ± 8	−906 ± 59	−280 ± 1	56 ± 5	−96 ± 1	314 ± 4
21-4	23-4	−241 ± 5	1488 ± 36	−409 ± 8	−946 ± 39	−430 ± 1	25 ± 9	−220 ± 1	571 ± 8
1-7	4-7	−294 ± 53	1585 ± 47	−1470 ± 55	847 ± 61	−559 ± 3	179 ± 8	−45 ± 2	380 ± 8
4-7[b]	8-7	−5868 ± 14	1967 ± 45	1524 ± 21	2408 ± 52	−795 ± 3	535 ± 4	−340 ± 3	607 ± 4
8-7[c]	11-7	−1150 ± 14	−258 ± 26	1938 ± 19	−547 ± 31	32 ± 1	−9 ± 3	30 ± 1	−62 ± 3
11-7[c]	15-7	−3929 ± 140	1448 ± 54	−528 ± 130	2991 ± 59	−792 ± 2	666 ± 4	−586 ± 2	703 ± 4
15-7	18-7	−1341 ± 97	2245 ± 75	−4535 ± 84	3643 ± 71	−1199 ± 7	1046 ± 5	−726 ± 8	881 ± 5
15-9	18-9	−305 ± 313	−4286 ± 616	2465 ± 243	2119 ± 579	−200 ± 17	36 ± 638	124 ± 12	35 ± 629
18-9[c]	22-9	1880 ± 262	975 ± 239	−540 ± 272	−2320 ± 274	−192 ± 6	−76 ± 23	24 ± 6	240 ± 22
22-9	25-9	−39 ± 5	7949 ± 65	−368 ± 6	−7550 ± 71	−577 ± 6	292 ± 11	−250 ± 6	530 ± 11
25-9	29-9	−31 ± 2	1139 ± 43	−369 ± 3	−734 ± 45	−285 ± 0	−45 ± 6	18 ± 0	307 ± 6
29-9	2-10	1138 ± 15	−1358 ± 39	379 ± 14	−146 ± 40	−253 ± 2	−28 ± 7	−19 ± 2	301 ± 6
28-10	31-10	−553 ± 12	2855 ± 18	−6251 ± 14	3877 ± 22	−2640 ± 26	−204 ± 57	−260 ± 24	3051 ± 55
31-10[c]	4-11	5683 ± 22	−1544 ± 12	−6673 ± 49	2598 ± 29	−4053 ± 20	2345 ± 12	1860 ± 13	−143 ± 4
4-11	6-11	−515 ± 36	−1118 ± 27	472 ± 58	1113 ± 57	−600 ± 32	256 ± 24	812 ± 5	−512 ± 5
1−12	5−12	−4637 ± 168	26652 ± 576	−2785 ± 124	−19320 ± 614	−1003 ± 6	193 ± 32	−1300 ± 6	2043 ± 32
5-12	8-12	3268 ± 11	−3496 ± 16	3018 ± 11	−2749 ± 15	−53 ± 1	−326 ± 2	49 ± 1	324 ± 2
8-12	11-12	6903 ± 17	−7494 ± 16	5329 ± 15	−4755 ± 16	1250 ± 6	−1184 ± 7	1435 ± 6	−1522 ± 6
Start	End	$Q^{U}_{y,3}$	$Q^{B}_{y,3}$	$Q^{U}_{y,2}$	$Q^{B}_{y,2}$	$Q^{s}_{Z,3}$	$Q^{n}_{Z,3}$	$Q^{s}_{Z,2}$	$Q^{n}_{Z,2}$
7-4[b]	10-4	3505 ± 365	1700 ± 239	58 ± 17	729 ± 86	−2578 ± 33	−1909 ± 53	−662 ± 12	−444 ± 11
10-4	14-4	−119 ± 8	228 ± 11	113 ± 4	62 ± 4	279 ± 6	−43 ± 8	204 ± 2	76 ± 2
14-4[c]	17-4	566 ± 11	936 ± 21	7 ± 0	−31 ± 4	255 ± 10	−421 ± 13	−102 ± 0	−109 ± 0
17-4	21-4	756 ± 18	135 ± 34	138 ± 3	65 ± 3	206 ± 20	−827 ± 25	−28 ± 2	−221.5 ± 2
21-4	23-4	794 ± 13	133 ± 19	310 ± 5	36 ± 4	784 ± 17	−838 ± 21	176 ± 5	−374 ± 6
1-7	4-7	130 ± 48	854 ± 49	190 ± 2	152 ± 8	351 ± 6	759 ± 13	31 ± 1	87 ± 1
4-7[b]	8-7	−3015 ± 13	−1167 ± 45	121 ± 3	131 ± 5	2527 ± 3	706 ± 8	283 ± 1	425 ± 1
8-7[c]	11-7	−1137 ± 11	−235 ± 24	−10 ± 1	−23 ± 3	39 ± 3	−772 ± 7	−98 ± 1	−105 ± 1
11-7[c]	15-7	−1495 ± 112	−1098 ± 55	10 ± 2	97 ± 5	1844 ± 28	1227 ± 20	385.2 ± 1	486 ± 1
15-7	18-7	1116 ± 54	−372 ± 76	61 ± 4	74 ± 5	1737 ± 42	2225 ± 29	525 ± 4	766 ± 4
15-9	18-9	−2071 ± 243	−2679 ± 531	41 ± 88	100 ± 713	−1643 ± 105	−595 ± 47	−308 ± 84	−161 ± 75
18-9[c]	22-9	1621 ± 299	970 ± 186	125 ± 9	131 ± 17	−235 ± 73	−1274 ± 104	6 ± 5	−69 ± 6
22-9	25-9	3480 ± 30	4151 ± 37	218 ± 11	41 ± 8	3268 ± 28	−3691 ± 34	215 ± 5	−0 ± 5
25-9	29-9	429 ± 16	349 ± 25	251 ± 1	65 ± 5	483 ± 17	−340 ± 19	68 ± 1	−197 ± 1
29-9	2-10	−315 ± 22	−193 ± 22	196 ± 4	73 ± 4	−1466 ± 21	−311 ± 22	52 ± 3	−171 ± 3
28-10	31-10	1381 ± 11	−1858 ± 20	667 ± 21	2113 ± 63	1662 ± 6	2223 ± 9	386 ± 9	1215 ± 10
31-10[c]	4-11	633 ± 15	1759 ± 12	834 ± 3	851 ± 15	−3160 ± 14	2013 ± 36	−1373 ± 13	2724 ± 20
4-11	6-11	−1801 ± 7	−128 ± 10	164 ± 3	133 ± 6	−477 ± 31	729 ± 59	−1008 ± 3	−67 ± 28
1-12	5-12	1447 ± 169	19840 ± 557	−266 ± 5	1024 ± 34	4769 ± 30	328 ± 59	685 ± 2	794 ± 2
5-12	8-12	−425 ± 5	−201 ± 8	−27 ± 0	395 ± 1	−3619 ± 10	−2624 ± 8	−259 ± 1	−169 ± 1
8-12	11-12	−315 ± 6	−191 ± 5	−78 ± 1	7 ± 2	−5782 ± 14	−3762 ± 13	−1446 ± 5	−1075 ± 5

[a]The fluxes notation is explained in the notation section. Values are in $m^3\ s^{-1}$. For the start and end dates, read 7-4 as 7 April.
[b]Fluxes matching the *Souto et al.* [2003] scheme.
[c]Fluxes similar to the *Souto et al.* [2003] scheme.

average temperature, and consequently decreasing the vertical gradients in the ria. Likewise the horizontal distributions (Figures 3b, 3c, 3e, and 3f) show signals of the upwelling enhanced residual circulation in the middle zone of the ria. The sea surface isohalines and isotherms lay diagonal to the main axis of the ria, reflecting the low river discharge flowing out through the northern side of the ria. The surface water in the middle and inner segments leaves the ria mainly by the northern side.

[44] The two sets of box model results (11−15 and 15−18 July) show a typical estuarine residual circulation pattern in two layers (Figure 4). The surface layer flowing shelfward (Figures 4a and 4c) is compensated by an inflow through the bottom layer that give rise to an upward flux through Z_C (Figures 4b and 4d). Another common feature in both results is the north-south asymmetry present in the horizontal fluxes through the wall separating boxes 2 and 3. In the outflowing upper layer the northern fluxes are larger than the southern ones and this explains the oblique disposition of the isohalines and isotherms found in the horizontal distributions (Figures 3b, 3c, 3e, and 3f). From 11 to 15 July the circulation scheme in box 3 shows a net inflow in the ria through the northern mouth that crosses the ria transversally and returns to the shelf through the upper layer of the southern mouth while an inflow flux is maintained through the bottom layer of the southern mouth. *Souto et al.* [2003] describes a very similar circulation pattern for an upwelling situation but with unidirectional inflow (flux in only one layer or the two layer fluxes flowing in the same sense) through the northern mouth.

4.1.2. Downwelling Event

[45] During the late autumn CTD campaign the Ekman transport perpendicular to the western Galician coast (E_x) was mainly downwelling favorable (Figure 2d) and the river runoff was high (Figure 2c) because of the wet season: higher precipitations (Figure 2c) and daily average temper-

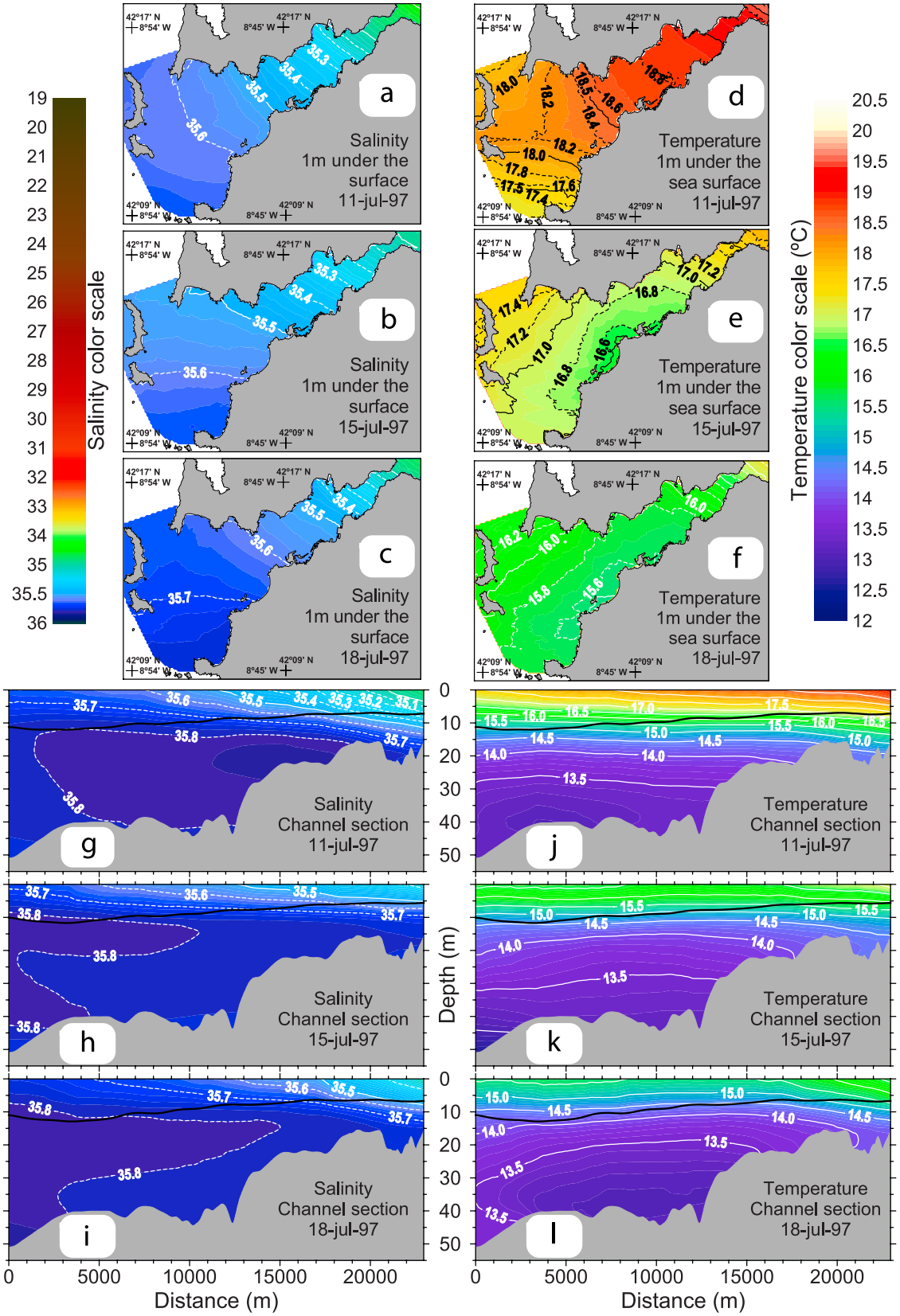

Figure 3. (left) Contours of salinity and (right) temperature from interpolated CTD data for the last three surveys of the Spring Campaign. (a–f) Contours at the surface (1 m under the surface). (g–l) Contours of the vertical section along the main channel transect (Figure 1).

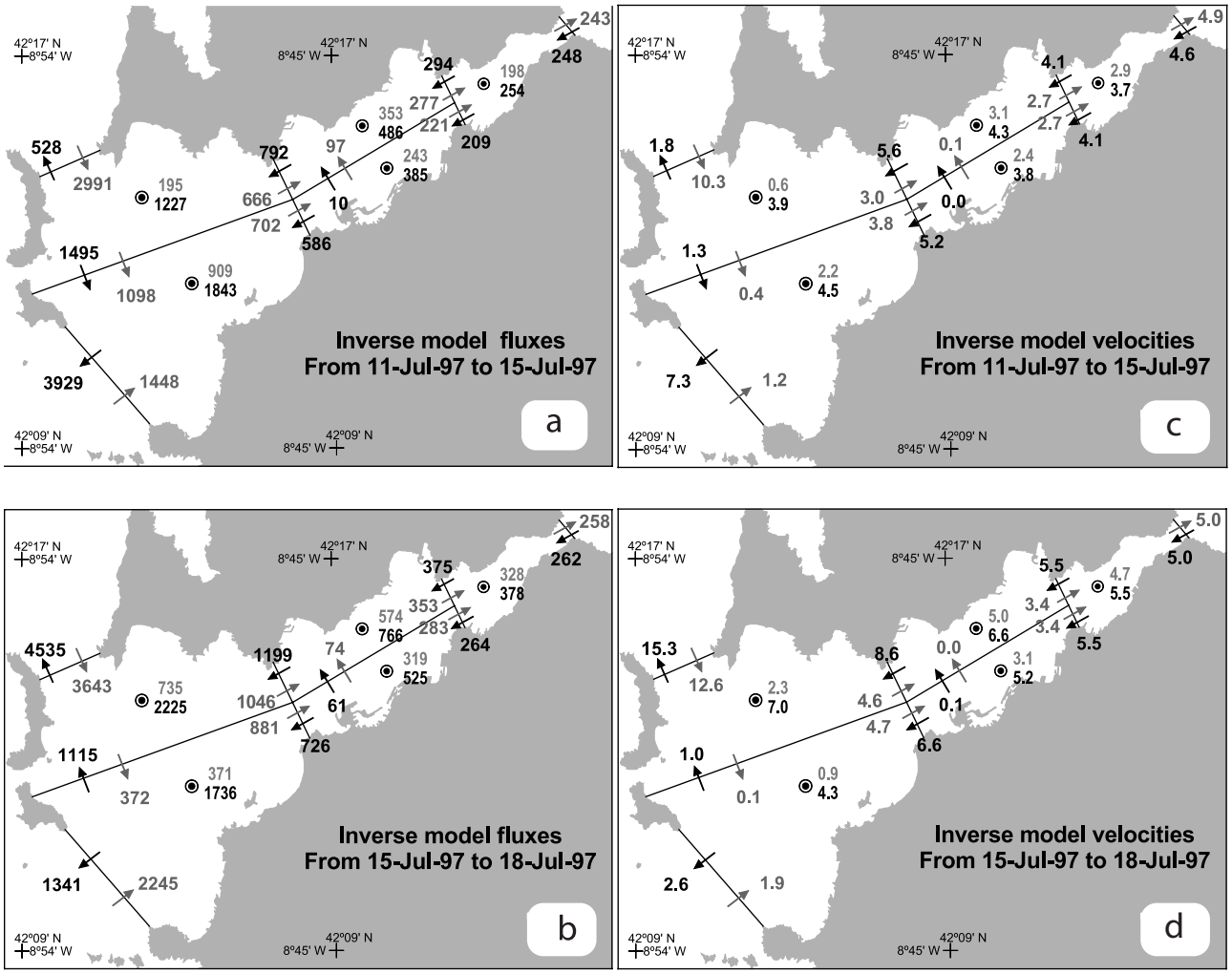

Figure 4. Fluxes (horizontal in $m^3\ s^{-1}$ and vertical in $10^3\ m^3\ s^{-1}$) obtained with the model inversions (a) from 11 to 15 July and (b) from 15 to 18 July and (c and d) the corresponding velocities (horizontal in $cm\ s^{-1}$ and vertical in $10^3\ cm\ s^{-1}$). Black arrows (values with black labels) indicate the direction of the flow in the upper layer, and gray arrows (values with gray labels) indicate the direction of flow in the bottom layer. The vertical upward advective fluxes (velocities) are marked with circled dots, and the downward are marked with $-\oplus$ values in black are the corresponding flux values, and the values in gray are the exchange coefficient values (in $10^3\ m^3\ s^{-1}$ and $10^3\ cm\ s^{-1}$).

ature between 12° and 18°C (Figure 2b). During the period between the three last surveys shelf winds indicate a moderate downwelling event (Figure 2d). The effects of downwelling in the temperature and salinity fields are shown in Figure 5 through contours of horizontal salinity distributions in the surface of the ria (Figures 5a–5c), salinity distributions on the bottom (the salinity at the bathymetry level, Figures 5d–5f), and vertical sections of salinity and temperature (Figures 5g–5l) along the main channel of the ria (dashed gray line in Figure 1).

[46] On 5 December the starting day of the downwelling event and the final day of a 5-day period without remote wind forcing (Figure 2d), the salinity field structure showed marked vertical gradients along the main channel of the ria (Figure 5g). The 35.8 (Figure 5g) and 35.9 (Figure 5d) isohalines portrayed an important volume of saline shelf water distributed from the southern mouth to the inner ria. The large river discharge creates an upper layer with salinities lower than 35 (Figure 5g) and intensifies the horizontal (along the main axis) salinity gradient (Figure 5a). The main feature shown by the temperature field was a clear inversion (Figure 5j), i.e., higher temperatures with increasing depth, due to the warm and salty shelf waters typical of this period of the year and the colder river waters. On the 8 December the spatial distributions of the thermohaline fields changed dramatically. An intense longitudinal gradient established in the surface of the head of the ria (Figure 5b). The 35.7 and saltier shelf water was flushed out of the ria (Figures 5e and 5h) with its corresponding warm pool of water (Figure 5k). The next survey, 11 December, the mean salinity and temperature of the ria were significantly lower (Figures 5c, 5f, 5i, and 5l). The water inside the ria kept flushing out by the deepest zones of the southern mouth while shelf surface waters entered the ria and accumulated fresh water in the inner zones. Since the water below the 35 isohaline (very shallow on 5 December, Figures 5d and 5g)

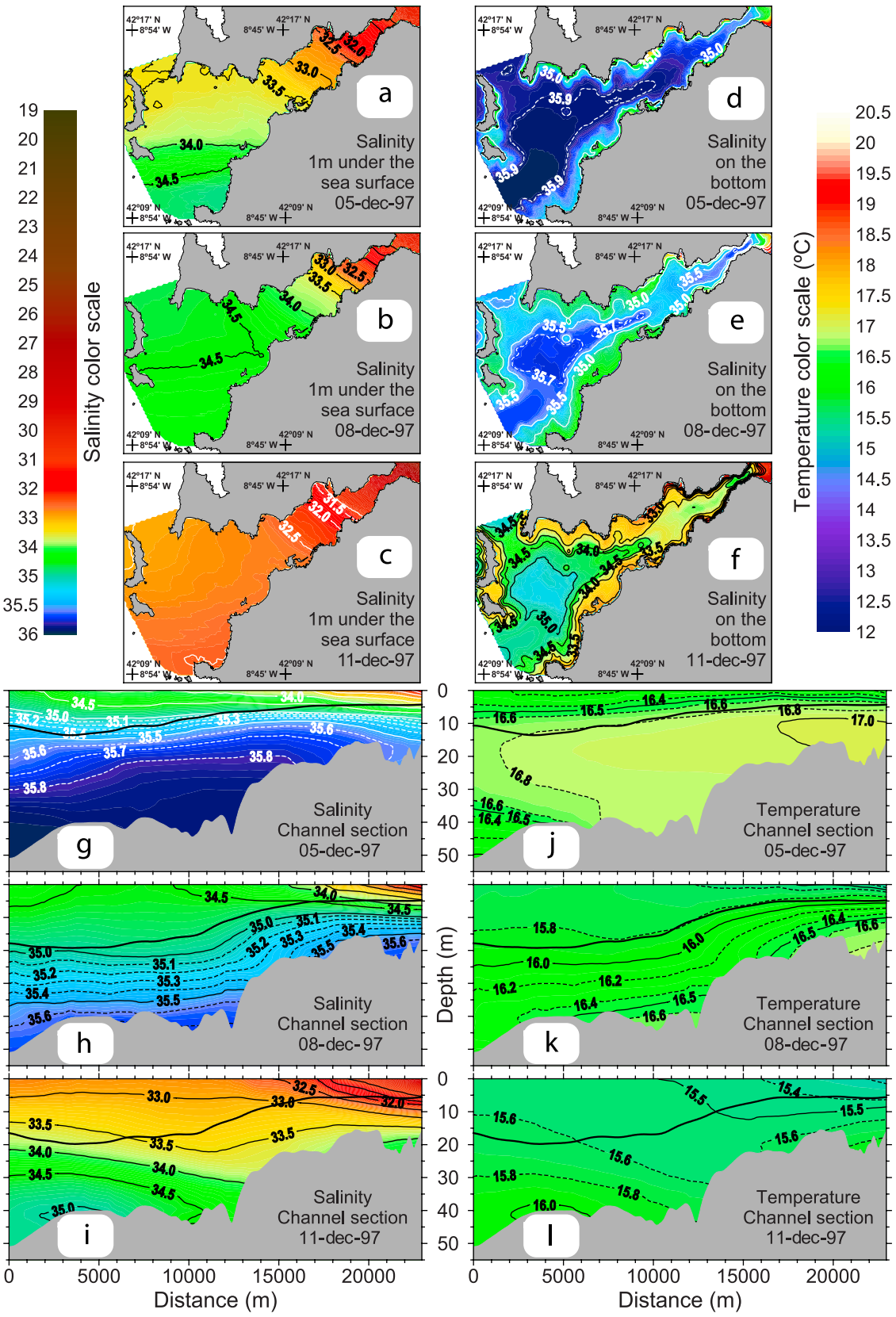

Figure 5. Contours of salinity and temperature from interpolated CTD data for the last three surveys of the late autumn campaign. (a–c) Salinity contours at the surface (1 m under the surface) and (d–f) salinity contours at the bottom level. (g–i) Salinity and (j–l) temperature contours of the vertical section along the main channel transect (Figure 1).

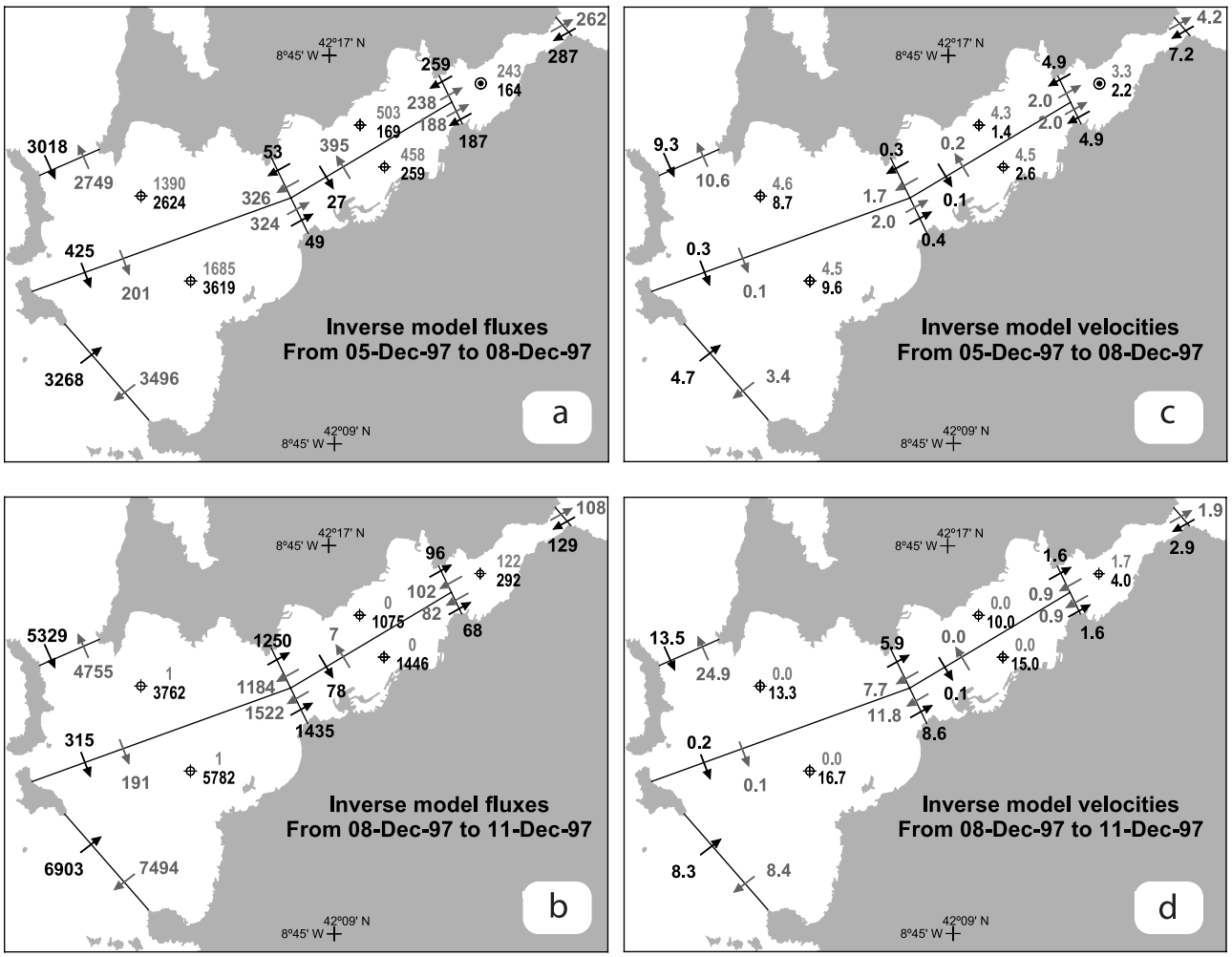

Figure 6. Fluxes (horizontal in $m^3\ s^{-1}$ and vertical in $10^3\ m^3\ s^{-1}$) obtained with the model inversions (a) from 5 to 8 December and (b) from 8 to 11 December and (c and d) the corresponding velocities (horizontal in cm s^{-1} and vertical in 10^3 cm s^{-1}). Black arrows (values with black labels) indicate the direction of the flow in the upper layer, and the gray arrows (values with gray labels) indicate the direction of the flow in the bottom layer. The vertical upward advective fluxes (velocities) are marked with circled dots, and the downward are marked with crossed circles; the values in black close to them are the corresponding flux values, and the values in gray are the exchange coefficient values (in $10^3\ m^3\ s^{-1}$ and 10^3 cm s^{-1}).

was reduced to a very small volume in the deepest parts of the ria (Figures 5f and 5i) on 11 December most of the volume of the ria was evacuated in 6 days showing the dramatic effect of the downwelling event.

[47] The two sets of results from the inverse model (5–8 and 8–11 December) show that the residual circulation was mainly in two layers but reversed (Figure 6). Shelf surface water entered the ria through the mouths by the upper layer, mixed with the continental runoff water, sunk, and, finally, returned to the shelf through the bottom layer. The first set of results is an exception to this general pattern because the residual circulation in the wall between boxes 2 and 3 was not structured in two horizontal layers but in two vertical layers (i.e., in the southern semiwalls there was an unidirectional inflowing flux and an unidirectional outflowing flux in the northern ones). This time the residual circulation inferred in box 3 did not follow the scheme proposed by *Souto et al.* [2003] because there was no coastal jet penetrating through the southern mouth and leaving the ria through the northern mouth. A possible explanation could be the fact that the downwelling event was moderate and significantly weaker than the downwelling events of October and November (Figure 2d).

4.2. Residual Circulation

4.2.1. Three-Dimensional Structure of the Residual Circulation

[48] Figures 4 and 6 show that only one of four residual circulation schemes obtained with the inverse model follows the pattern proposed by *Souto et al.* [2003]. In fact, checking Table 1, it is possible to find two results of the inverse model that exactly match the proposed residual circulation scheme and five very similar to it. Thus 7 of 21 sets of results follow the Souto et al. scheme. It should be

Table 2. Correlation Coefficients Among Advective Fluxes[a]

	${}^2Q^{U}_{x,3}$	${}^2Q^{U,s}_{x,3}$	${}^2Q^{B,s}_{x,3}$	${}^2Q^{U,n}_{x,3}$	${}^2Q^{B,n}_{x,3}$	${}^1Q^{U}_{x,3}$	${}^1Q^{U,n}_{x,3}$	${}^1Q^{B,n}_{x,3}$	${}^1Q^{U,s}_{x,3}$	${}^1Q^{B,s}_{x,3}$	$Q^{s}_{Z,3}$	$Q^{n}_{Z,3}$	$Q_{Z,3}$	$Q^{s}_{Z,2}$	$Q^{n}_{Z,2}$
${}^2Q^{U,s}_{x,3}$	0.77	1													
${}^2Q^{B,s}_{x,3}$	−0.64	−0.54	1												
${}^2Q^{U,n}_{x,3}$	0.69	0.08	−0.38	1											
${}^2Q^{B,n}_{x,3}$	−0.07	0.01	−0.73	−0.12	1										
${}^1Q^{U}_{x,3}$	**0.90**	0.52	−0.56	**0.83**	−0.08	1									
${}^1Q^{U,n}_{x,3}$	0.60	0.08	−0.21	**0.86**	−0.26	**0.82**	1								
${}^1Q^{B,n}_{x,3}$	−0.56	−0.24	0.15	−0.61	0.31	−0.66	−0.79	1							
${}^1Q^{U,s}_{x,3}$	0.64	0.78	−0.65	0.12	0.27	0.47	−0.12	0.07	1						
${}^1Q^{B,s}_{x,3}$	−0.77	−0.50	0.62	−0.63	−0.12	**−0.82**	−0.49	0.12	−0.68	1					
$Q^{s}_{Z,3}$	**−0.86**	**−0.86**	0.77	−0.38	−0.23	−0.66	−0.22	0.26	**−0.81**	0.67	1				
$Q^{n}_{Z,3}$	−0.78	−0.46	0.18	−0.70	0.46	−0.74	−0.71	0.65	−0.19	0.48	0.38	1			
$Q_{Z,3}$	**−0.99**	**−0.83**	0.63	−0.61	0.06	**−0.83**	−0.5	0.51	−0.66	0.71	**0.89**	0.76	1		
$Q^{s}_{Z,2}$	−0.71	−0.77	0.58	−0.23	−0.13	−0.57	−0.02	0.05	−0.96	0.73	**0.83**	0.28	0.72	1	
$Q^{n}_{Z,2}$	−0.61	−0.13	0.28	**−0.81**	0.18	**−0.81**	**−0.97**	**0.84**	0.08	0.44	0.23	0.71	0.52	0.04	1
$Q_{Z,2}$	**−0.90**	−0.56	0.56	−0.78	0.07	**−0.98**	−0.77	0.69	−0.50	0.77	0.68	0.72	**0.83**	0.62	**0.81**

[a]The significant correlation coefficient is at 99% confidence level, and 19 degrees of freedom is 0.549. The values greater than or equal to |±0.80| are bold. The flux notation is explained in the notation section and in the text (section 4.2.1).

noted that Souto et al.'s scheme was deduced from observational data (∼2 months of current meter time series), numerical simulations, and theoretical grounds but the scheme was presented with a simulation with idealized smooth-time-varying wind conditions. So under real oceanographic and meteorological conditions the Souto et al. scheme should present variations. Also, taking into account the diverse situations covered by the five campaigns (upwelling, downwelling, relaxation and spin-up of upwelling and downwelling), the spatial average nature of the estimated fluxes, and that sometimes the time interval between surveys is larger than 3 days, the ratio 7:21 is significant and should be considered as a verification of the Souto et al. scheme.

[49] Table 2 compiles the correlation coefficients among inverse model advective fluxes: the horizontal fluxes in both mouths (upper northern ${}^2Q^{U,n}_{x,3}$ and southern ${}^2Q^{U,s}_{x,3}$, bottom northern ${}^2Q^{B,n}_{x,3}$ and southern ${}^2Q^{B,s}_{x,3}$) and its upper advective net flux (${}^2Q^{U}_{x,3} = {}^2Q^{U,s}_{x,3} + {}^2Q^{U,n}_{x,3}$); in the wall between boxes 2 and 3 (upper northern ${}^1Q^{U,n}_{x,3}$ and southern ${}^1Q^{U,s}_{x,3}$, bottom northern ${}^1Q^{B,n}_{x,3}$ and southern ${}^1Q^{B,s}_{x,3}$) and its upper advective net flux (${}^1Q^{U}_{x,3} = {}^1Q^{U,s}_{x,3} + {}^1Q^{U,n}_{x,3}$); the vertical advective fluxes in box 3 (northern $Q^{n}_{Z,3}$ and southern $Q^{s}_{Z,3}$ semiboxes) and its vertical net flux ($Q_{Z,3} = Q^{n}_{Z,3} + Q^{s}_{Z,3}$); and the vertical fluxes in box 2 (northern $Q^{n}_{Z,2}$ and southern $Q^{s}_{Z,2}$ semiboxes, and vertical net $Q_{Z,2} = Q^{n}_{Z,2} + Q^{s}_{Z,2}$). The correlation coefficients must be interpreted under the sign convention established for the horizontal (negative when the flow is seaward and positive if the flow is into the ria) and vertical (negative downward and positive upward) fluxes.

[50] From a 2-D point of view, the set of 3-D solutions of the inverse model keeps the coherence with a two-layer estuarine dynamic because the net upper flux in the mouths (${}^2Q^{U}_{x,3}$) correlates with the net upper flux of the wall between boxes 2 and 3 (${}^1Q^{U}_{x,3}$) and both correlate with the vertical fluxes in boxes 2 and 3. Thus the classical 2-D residual circulation scheme endures under the 3-D variations. However, the most interesting points of Table 2 should be observed from a 3-D point of view. For example, the water entering (leaving) the ria through the upper northern mouth usually pass through the upper northern box 2−box 3 wall since ${}^2Q^{U,n}_{x,3}$ correlates with ${}^1Q^{U}_{x,3}$ and with ${}^1Q^{U,n}_{x,3}$ but not with ${}^1Q^{U,s}_{x,3}$. On the other hand, the bottom northern mouth flux (${}^2Q^{B,n}_{x,3}$) only correlates with the bottom southern mouth flux (${}^2Q^{B,s}_{x,3}$), i.e., when the water enters the ria through the bottom of the southern mouth usually leaves the ria through the bottom of the northern mouth and, conversely, when it leaves the ria through the bottom of the southern mouth it usually enters by the bottom of the northern mouth.

[51] Since the cross-sectional area of the southern mouth is larger than the northern mouth, it is expected that the exchange with the shelf through the upper layer (${}^2Q^{U}_{x,3}$) correlates with the southern fluxes (${}^2Q^{U,s}_{x,3}$ and ${}^2Q^{B,s}_{x,3}$) better than with the northern ones (${}^2Q^{U,n}_{x,3}$ and ${}^2Q^{B,n}_{x,3}$). This asymmetry is also maintained in the wall between boxes 2 and 3, since the correlation between ${}^2Q^{U}_{x,3}$ and the southern fluxes (${}^1Q^{U,s}_{x,3}$ and ${}^1Q^{B,s}_{x,3}$) is higher than with the northern fluxes (${}^1Q^{U,n}_{x,3}$ y ${}^1Q^{B,n}_{x,3}$). Another interesting feature affecting the box 2−box 3 wall is that the water usually enters (leaves) the ria through the bottom southern semiwall and leaves (enters) the ria through the upper northern semiwall as is indicated by the higher correlation between the net upper flux (${}^1Q^{U}_{x,3}$) with these semiwalls (${}^1Q^{B,s}_{x,3}$ and ${}^1Q^{U,n}_{x,3}$).

4.2.2. Residual Circulation Forcing and Its Barotropic Bidirectional Flow

[52] The influence of the remote forcing by means of the component of the Ekman transport perpendicular to the western Galician coast has been extensively documented [*Álvarez-Salgado et al.*, 2000] in several Galician rias: by *Rosón et al.* [1997] in the Arousa Ria, *Pardo et al.* [2001] in the Pontevedra Ria, and *Gilcoto et al.* [2001], *Míguez et al.* [2001], and *Míguez et al.* [2001] in the Ría de Vigo. Recently, *Souto et al.* [2003] and *Piedracoba et al.* [2005] have shown with numerical simulations, current meters and CTD surveys that remote wind controls very frequently the residual circulation of the ria through coastal upwelling/downwelling events. Indeed, these studies show that this control reaches the diurnal and higher frequencies of the velocity spectrum and the lagged response of the residual circulation of the ria to shelf wind is very fast (from 6 hours to 2 days depending on the wind characteristics and oceanographic conditions).

[53] Therefore, in the analysis of the forces driving the residual exchange fluxes (Table 1) between the shelf and the

Table 3. Mean Values Between CTD Surveys of Daily Forcing Values[a]

Start	End	$\Delta_y\rho$, kg m^{-3}	$\Delta_x\rho$, kg m^{-3}	$\Delta_z\rho$, kg m^{-3}	E_x, m^3 s^{-1} km^{-1}	E_y, m^3 s^{-1} km^{-1}	W_p, m s^{-1}	W_t, m s^{-1}
7 Apr	10 Apr	−0.03	−0.34	−0.36	−29.3	−33.1	0.63	−0.30
10 Apr	14 Apr	−0.04	−0.28	−0.44	−167.6	−21.0	0.30	−0.30
14 Apr	17 Apr	−0.05	−0.28	−0.62	−9.9	−15.5	0.58	−0.25
17 Apr	21 Apr	−0.02	−0.33	−0.70	−375.1	145.8	−0.65	0.32
21 Apr	23 Apr	−0.03	−0.29	−0.60	−611.9	180.5	−1.46	−0.25
1 Jul	4 Jul	−0.09	−0.77	−1.20	−186.5	−194.7	0.82	−1.36
4 Jul	8 Jul	−0.05	−0.59	−0.98	−391.3	33.5	−0.86	−0.75
8 Jul	11 Jul	−0.06	−0.55	−0.93	−24.9	−99.8	1.45	−0.35
11 Jul	15 Jul	−0.06	−0.50	−0.88	−509.1	83.3	−0.56	−0.70
15 Jul	18 Jul	−0.05	−0.33	−0.57	−886.0	237.9	−0.65	−0.31
15 Sep	18 Sep	−0.05	−0.17	−0.38	−8.9	−13.3	0.62	−0.14
18 Sep	22 Sep	−0.04	−0.04	−0.38	−69.9	−41.5	0.87	−0.17
22 Sep	25 Sep	−0.03	0.02	−0.33	−24.9	−9.7	0.66	0.04
25 Sep	29 Sep	−0.05	0.97	−0.36	−95.0	6.9	0.40	−0.04
29 Sep	2 Oct	−0.06	1.29	−0.37	−124.0	2.0	0.39	0.00
28 Oct	31 Oct	−0.11	−0.67	−0.87	−169.2	−40.5	0.14	−0.50
31 Oct	4 Nov	−0.06	−0.47	−0.46	219.1	79.4	−0.58	0.45
4 Nov	6 Nov	0.01	−0.53	−0.40	149.2	−122.8	1.34	0.44
1 Dec	5 Dec	−0.20	−0.94	−2.01	−51.8	−25.7	−1.13	−0.32
5 Dec	8 Dec	−0.06	−0.50	−0.81	502.1	126.9	0.18	0.49
8 Dec	11 Dec	−0.04	−0.70	−0.87	573.8	−159.0	1.34	−0.68

[a]See the text (section 4.2.2) for variable notation.

ria we have taken in account (Table 3) the remote wind in Ons Island (Ekman transports, E_x and E_y), the local wind in Bouzas station (W_t and W_p), and the density gradients ($\Delta\rho$). The density gradient along the longitudinal axis of the ria ($\Delta_x\rho$) has been estimated with the difference between the volume average densities in boxes 1 and 3, the transversal density gradient ($\Delta_y\rho$) with the difference between the volume average densities in the northern and southern semiboxes of box 3, and the vertical density gradient ($\Delta_z\rho$) with the difference of the upper and bottom density semiboxes of box 3. The forcing analysis has been done with multiparametric linear regressions of the net upper flux in the mouths of the ria ($Q_{Mouths} = {}^2Q^U_{x,3} = {}^2Q^{U,n}_{x,3} + {}^2Q^{U,s}_{x,3}$) against the variables shown in Table 3 plus the river discharge and the time variation of the subtidal sea surface. The two latter forcing mechanisms did not explain any significant part of the variance and, therefore they were not included in Table 3. In order to propagate the estimated errors of the inverse model to the multiparametric regressions (equations (32) and (33)), we have chosen the Weighted Least Squares, with the sum of the errors of the fluxes at the mouths as weights, to perform the multiparametric analysis.

[54] The best fit found between Q_{Mouths} and the forcing variables is expressed with equation (32). This regression has a determination coefficient of $r^2 = 0.75$ (its probability of rejection with 14 degrees of freedom is P(14 df) < 0.001) and the partial correlation coefficients for each forcing are shown in Table 4.

$$Q_{Mouths} = (99.8 \pm 23.9)\cdot 10^3\cdot\Delta_y\rho - (3.5 \pm 3.6)\cdot 10^3 \cdot\Delta_x\rho - (5.5 \pm 2.5)\cdot 10^3\cdot\Delta_z\rho + (8.8 \pm 1.9) \cdot E_x + (19.1 \pm 5.1)\cdot E_y + (0.9 \pm 1.1)\cdot 10^3 \cdot W_p - (4.2 \pm 1.4)\cdot 10^3\cdot W_t \quad (32)$$

[55] The local wind parallel to the axis of the ria and the longitudinal density gradient were dropped since their rejection probabilities were higher than 0.05 (Table 4) and a new multiparametric fit was estimated:

$$Q_{Mouths} = (87.3 \pm 20.1)\cdot 10^3\cdot\Delta_y\rho - (7.5 \pm 1.8)\cdot 10^3\cdot\Delta_z\rho + (9.9 \pm 1.3)\cdot E_x + (16.2 \pm 3.7)\cdot E_y - (4.6 \pm 1.3) \cdot 10^3\cdot W_t \quad (33)$$

[56] In the last equation ($r^2 = 0.76$, P(16 df) < 0.0001) the Ekman transport has the higher partial correlation coefficient (Table 4), an evidence of its large influence on the residual circulation. The coefficients in equation merit attention in order to evaluate the physical feasibility and meaning of the equation (33). The magnitude of the Ekman transport coefficients (9.9 and 16.2 km) are of the order of the sum of the length of the mouths (9.5 km, southern plus northern). The coefficient of the transversal density gradient, which is the second most important forcing (Table 4), suggests that the baroclinic coupling is active mainly through geostrophic dynamics (i.e., the transversal density gradient is not negligible in the longitudinal component of the dynamic balance). A geostrophic dynamic could be possible because a timescale of about 2 days is obtained from a 10 cm s^{-1} residual velocity scale and a ria length

Table 4. Partial Correlation Coefficients (Partial r) and Rejection Probabilities (P) for Each Forcing Mechanism in the Multiparametric Fit of Net Ria-Shelf Exchange Fluxes[a]

	Equation (32)		Equation (33)	
	Partial r	P (14 df)	Partial r	P(16 df)
$\Delta_y\rho$	0.74	<0.001	0.72	<0.001
$\Delta_x\rho$	−0.25	0.352	–	–
$\Delta_z\rho$	−0.51	0.045	−0.72	<0.001
Q_x	0.78	<0.001	0.88	<0.001
Q_y	0.70	0.002	0.74	<0.001
W_p	0.22	0.406	–	–
W_t	−0.63	0.009	−0.67	0.002

[a]Here df indicates degrees of freedom.

scale of 20 km (10 cm s^{-1}/20 km = 2.31 days). The geostrophic along channel velocity (u_g) and its associated advective flux are

$$u_g = \frac{g \cdot h}{f \cdot \rho} \cdot \frac{\partial \rho}{\partial y} \approx \frac{g \cdot h}{f \cdot \rho} \cdot \frac{\Delta_y \rho}{\Delta y} \tag{34}$$

The last expression represents the component along the ria channel of the thermal wind balance; g is the gravity acceleration, f the Coriolis factor, ρ the density, h the mean depth of box 3, Δy the distance between the northern and southern semiboxes of box 3 and $\Delta_y \rho$ has been defined previously in this section. The associated flux in a mean cross section of box 3 (with area $h \cdot 2 \cdot \Delta y$) is

$$\begin{aligned} Q_g &= u_g \cdot h \cdot 2 \cdot \Delta y = B \cdot \Delta_y \rho \\ B &= \frac{2 \cdot g \cdot h^2}{f \cdot \rho} \end{aligned} \tag{35}$$

Recalling the regression coefficient $B \sim 87.3 \cdot 10^3$ and with the Coriolis factor at 42.22° north ($f = 9.77 \times 10^{-5}$ s^{-1}), the gravity acceleration ($g = 9.8$ m s^{-2}) and a mean density ($\rho \sim 1025$ kg m^{-3}) we obtain a mean depth of $h \sim 21$ m for box 3, again an appropriate value. The evaluation of the coefficient of the vertical density gradient ($\sim -7.5 \times 10^3$ kg^{-1} s^{-1}) is more difficult, but multiplying it by the mean vertical density gradient (~ -0.54 kg m^{-3}), we obtain a reasonable vertical flux of $\sim 4.1 \times 10^3$ m^3 s^{-1}. Finally, the local wind coefficient is negative and this means that southerly winds (positive) generate a negative flux (seaward). When the fresher and lighter water of continental origin is dragged northward by local wind, the transversal density gradient and its associated geostrophic current are enhanced.

[57] Another question is the bidirectional structure of the barotropic residual circulation induced by remote wind. Until now, the bidirectional residual flow in estuaries and embayments has been mainly associated with the gravitational circulation or with local wind [*Hansen and Rattray*, 1965; *Officer*, 1976]. The paradigm of remote wind forcing is the generation of an unidirectional residual flow through variation of the sea level and conservation of volume [*Garvine*, 1985]. Indeed, when a bidirectional residual flow modulated by upwelling/downwelling processes has been found, for example by *Hickey et al.* [2002] and *Monteiro and Largier* [1999], the mechanism that has been invoked to explain the modulation is baroclinic. Upwelling/downwelling events modify the density in the mouth of the estuary/embayment thus changing the longitudinal density gradient and the associated gravitational circulation. In the Ría de Vigo, the barotropic character of the residual circulation is strong since the along axis density gradient has been rejected (from equation (32) to equation (33)) because it did not explain a significant percentage of variance of Q_{Mouths}. Indeed, the downwelling event described in section 4.1.2 also supports the barotropic hypothesis because the residual circulation (as given by the model estimations (Table 1) and the observed salinity and temperature fields (section 4.1.2)) flowed against the gravitational circulation, when the longitudinal gradient was large (Table 3). This point is surprising in an estuary because it is supposed that the gravitational circulation is one of the most important forcing in estuaries and rias.

[58] With the aid of the inverse model we have observed barotropic bidirectional flows driven by remote winds in the southern and northern mouths. The bidirectional vertical structure should depend on the thickness of the Ekman depth of upwelling in shelf. If the shelf surface layer induced by the wind is shallower than the water depth at the mouth of the ria, a barotropic bidirectional flow will develop. That is, the barotropic bidirectional flow induced in the ria is an extension of the two layer circulation on the shelf explained by the *Sverdrup* [1938] coastal upwelling theory. Certainly, more processes and more complex current patterns like those found at the Coastal Boundary Layer, Coastal Trapped Waves or the modulations induced in the upwelling by the density variations should account for the unexplained variance of our linear multiparametric equation (33).

[59] In the Garvine's [*Garvine*, 1985; *Janzen and Wong*, 2002] or Wong's [*Kasai et al.*, 2000; *Wong*, 1994] theoretical models of residual circulation forced by remote wind, the imposed volume boundary condition is that the sea level variations are proportional to the shelf wind stress. In this sense, the only possible flow structure at the shelf-estuary connection generated by the remote winds is a barotropic unidirectional flow. Then, in those models the unidirectional flow forced by remote wind is a consequence of the a priori imposed volume boundary condition and not a result of the theoretical model. This means that the residual circulation driven by remote wind in the Ría de Vigo must not be interpreted in the context of such theoretical models, because coastal upwelling can impose a bidirectional circulation of barotropic origin that is impossible to achieve with the volume boundary condition of these theoretical models.

5. Conclusions

[60] An inverse model has been applied to the Ría de Vigo. The design of the model was inspired by the existence of a 3-D residual circulation in the outer segment of the ria. Another improvement in the design of the model has been the fact that the inverse method used finds optimal solutions constrained with the condition of non negative vertical exchange coefficients.

[61] It should be noted that the inverse model does not contain any dynamic balance. The model is purely kinematic and it works with tracer and volume balances. Therefore the model limitations are those derived from the simplifications done in the tracer budget equations but it is greatly free from dynamic constraints imposed with simplified dynamic balances. This point is crucial for searching the main forces driving the residual circulation because there is not any forcing included a priori in the model equations.

[62] The inverse model results confirm again the large influence of remote wind forcing in the residual circulation of the ria and suggest geostrophic dynamics through density gradients and local wind. They also show that the two-layer circulation induced by the shelf dynamics is understood under a barotropic context, i.e., a barotropic bidirectional flow is induced by the Ekman transport acting on the shelf.

[63] Finally, it was observed that there is a 3-D residual circulation structure in addition to the classical 2-D. The 3-D residual circulation scheme in the mouths of the ria

proposed by *Souto et al.* [2003] extends to the interior of the ria. The existence of transversal variations in the flows in the middle ria was observed and it has clear implications for the residual circulation and thus for the flushing time of tracers in the ria.

Appendix A: Box Model Equations

[64] The system of subscripts and superscripts used in the notation of the variables (notation section) is complicated. The principal script is the numerical right subscript, it defines the actual box. The other scripts are referred to it and indicate where the variable is applied (upper (U), bottom (B), northern (n) or southern (s) semibox, semiwall, or surface). For example, in Figure 1 a vertical section of the southern semiboxes (upper and bottom) of box 2 is shown, so the numerical on the right subscript is "2", and the right superscript is a "s" (southern), the fluxes applied in the upper layer have "U" as superscript on the right, those applied in the bottom layer a "B" as superscript on the left, the fluxes of the seaward wall have a "2" as superscript on the left and those of the inner wall have a "1". The advective fluxes (Q_y) that cross the walls along the central axis of the ria are positive to the north, the horizontal fluxes (Q_x) that cross the walls perpendicular to the axis of the ria are positive seaward (westward) and the vertical advective fluxes (Q_Z) are positive when the flow is upward. The subtidal sea level is considered horizontal flat in whole ria, in the four boxes, so η has no scripts. Only the conservation equations of a dummy tracer (d) and the volume conservation equations are shown. The dummy tracer equations are used as templates for the conservation of mass ($d = \rho$), thermal energy ($d = \alpha$), and salt ($d = \upsilon$).

A1. Box 0: Two Unknowns and Four Equations

[65]

$$ {}^2Q^U_{x,0} + {}^2\,Q^B_{x,0} = Q_{E,0} - Q_{R,0} - Q_{L,0} + A_{\mathrm{sup},0}\cdot\frac{\Delta\eta}{\Delta t} \tag{A1}$$

$$ {}^2Q^U_{x,0}\cdot{}^2d^U_{x,0} + {}^2Q^B_{x,0}\cdot{}^2d^B_{x,0} = \overline{V}_0\cdot\frac{\Delta d_0}{\Delta t} + A_{\mathrm{sup},0}\cdot\frac{\Delta(d_0\cdot\eta)}{\Delta t} + SS(d)_0 \tag{A2}$$

A2. Box 1: Two Semiboxes, Four Unknowns, Eight Equations, and Two Boundary Conditions

[66] Boundary conditions

$$ {}^1Q^U_{x,1} = {}^2\,Q^U_{x,0} \qquad {}^1Q^B_{x,1} = {}^2\,Q^B_{x,0} \tag{A3}$$

[67] Upper semibox

$$ {}^2Q^U_{x,1} + Q_{Z,1} = Q_{E,1} - Q_{R,1} - Q_{L,1} + {}^1Q^U_{x,1} + \frac{\Delta\breve{V}^U_1}{\Delta t} + A_{\mathrm{sup},1}\cdot\frac{\Delta\eta}{\Delta t} \tag{A4}$$

$$ {}^2Q^U_{x,1}\cdot{}^2d^U_{x,1} + Q_{Z,1}\cdot d_{Z_C,1} - M_{Z,1}\cdot\left(d^U_1 - d^B_1\right) = {}^1Q^U_{x,1}\cdot{}^1d^U_{x,1} + \frac{\Delta\left(\breve{V}^U_1\cdot d^U_1\right)}{\Delta t} + A_{\mathrm{sup},1}\cdot\frac{\Delta\left(\eta\cdot d^U_1\right)}{\Delta t} + SS(d)_1 \tag{A5}$$

[68] Bottom semibox

$$ {}^2Q^B_{x,1} - Q_{Z,1} = {}^1Q^B_{x,1} + \frac{\Delta V^B_1}{\Delta t} \tag{A6}$$

$$ {}^2Q^B_{x,1}\cdot{}^2d^B_{x,1} - Q_{Z,1}\cdot d_{Z_C,1} + M_{Z,1}\cdot\left(d^U_1 - d^B_1\right) = {}^1Q^B_{x,1}\cdot{}^1d^B_{x,1} + \frac{\Delta\left(V^B_1\cdot d^B_1\right)}{\Delta t} \tag{A7}$$

A3. Box 2: Four Semiboxes, Eight Unknowns, 16 Equations, and Four Boundary Conditions

[69] Boundary conditions

$$ \begin{aligned} {}^1Q^{U,n}_{x,2} &= {}^2Q^U_{x,1}\cdot\frac{A^{U,n}_{x,2}}{A^U_{x,2}} \\ {}^1Q^{U,s}_{x,2} &= {}^2Q^U_{x,1}\cdot\frac{A^{U,s}_{x,2}}{A^U_{x,2}} \\ {}^1Q^{B,n}_{x,2} &= {}^2Q^B_{x,1}\cdot\frac{A^{B,n}_{x,2}}{A^B_{x,2}} \\ {}^1Q^{B,s}_{x,2} &= {}^2Q^B_{x,1}\cdot\frac{A^{B,s}_{x,2}}{A^B_{x,2}} \end{aligned} \tag{A8}$$

[70] Upper northern semibox

$$ {}^2Q^{U,n}_{x,2} + Q^n_{Z,2} + Q^U_{y,2} = Q^n_{E,2} - Q^n_{R,2} - Q^n_{L,2} + {}^1Q^{U,n}_{x,2} + \frac{\Delta\breve{V}\,5^{U,n}_2}{\Delta t} + A^n_{\mathrm{sup},2}\cdot\frac{\Delta\eta}{\Delta t} \tag{A9}$$

$$ {}^2Q^{U,n}_{x,2}\cdot{}^2d^{U,n}_{x,2} + Q^n_{Z,2}\cdot d^n_{Z_C,2} - M^n_{Z,2}\cdot\left(d^{U,n}_2 - d^{B,n}_2\right) + Q^U_{y,2}\cdot d^U_{y,2} = {}^1Q^{U,n}_{x,2}\cdot{}^1d^{U,n}_{x,2} + \frac{\Delta\left(\breve{V}^{U,n}_2\cdot d^{U,n}_2\right)}{\Delta t} + A^n_{\mathrm{sup},2}\cdot\frac{\Delta\left(\eta\cdot d^{U,n}_2\right)}{\Delta t} + SS(d)^n_2 \tag{A10}$$

[71] Upper southern semibox

$$ {}^2Q^{U,s}_{x,2} + Q^s_{Z,2} - Q^U_{y,2} = Q^s_{E,2} - Q^s_{R,2} - Q^s_{L,2} + {}^1Q^{U,s}_{x,2} + \frac{\Delta\breve{V}^{U,s}_2}{\Delta t} + A^s_{\mathrm{sup},2}\cdot\frac{\Delta\eta}{\Delta t} \tag{A11}$$

$$ {}^2Q^{U,s}_{x,2}\cdot{}^2d^{U,s}_{x,2} + Q^s_{Z,2}\cdot d^s_{Z_C,2} - M^s_{Z,2}\cdot\left(d^{U,s}_2 - d^{B,s}_2\right) - Q^U_{y,2}\cdot d^U_{y,2} = {}^1Q^{U,s}_{x,2}\cdot{}^1d^{U,s}_{x,2} + \frac{\Delta\left(\breve{V}^{U,s}_2\cdot d^{U,s}_2\right)}{\Delta t} + A^s_{\mathrm{sup},2}\cdot\frac{\Delta\left(\eta\cdot d^{U,s}_2\right)}{\Delta t} + SS(d)^s_2 \tag{A12}$$

[72] Bottom northern semibox

$$ {}^{2}Q^{B,n}_{x,2} - Q^{n}_{Z,2} + Q^{B}_{y,2} = {}^{1}Q^{B,n}_{x,2} + \frac{\Delta V^{B,n}_{2}}{\Delta t} \tag{A13} $$

$$ {}^{2}Q^{B,n}_{x,2} \cdot {}^{2}d^{B,n}_{x,2} - Q^{n}_{Z,2} \cdot d^{n}_{Z_C,2} + M^{n}_{Z,2} \cdot \left(d^{U,n}_{2} - d^{B,n}_{2}\right) + Q^{B}_{y,2} \cdot d^{B}_{y,2} = {}^{1}Q^{B,n}_{x,2} \cdot {}^{1}d^{B,n}_{x,2} + \frac{\Delta\left(V^{B,n}_{2} \cdot d^{B,n}_{2}\right)}{\Delta t} \tag{A14} $$

[73] Bottom southern semibox

$$ {}^{2}Q^{B,s}_{x,2} - Q^{s}_{Z,2} - Q^{B}_{y,2} = {}^{1}Q^{B,s}_{x,2} + \frac{\Delta V^{B,s}_{2}}{\Delta t} \tag{A15} $$

$$ {}^{2}Q^{B,s}_{x,2} \cdot {}^{2}d^{B,s}_{x,2} - Q^{s}_{Z,2} \cdot d^{s}_{Z_C,2} + M^{s}_{Z,2} \cdot \left(d^{U,s}_{2} - d^{B,s}_{2}\right) - Q^{B}_{y,2} \cdot d^{B}_{y,2} = {}^{1}Q^{B,s}_{x,2} \cdot {}^{1}d^{B,s}_{x,2} + \frac{\Delta\left(V^{B,s}_{2} \cdot d^{B,s}_{2}\right)}{\Delta t} \tag{A16} $$

A4. Box 3: Four Semiboxes, Eight Unknowns, 16 Equations, and Four Boundary Conditions

[74]

$$ \begin{aligned} {}^{1}Q^{U,n}_{x,3} &= {}^{2}Q^{U}_{x,2} \\ {}^{1}Q^{U,s}_{x,3} &= {}^{2}Q^{U}_{x,2} \\ {}^{1}Q^{B,n}_{x,3} &= {}^{2}Q^{B}_{x,2} \\ {}^{1}Q^{B,s}_{x,3} &= {}^{2}Q^{B}_{x,2} \end{aligned} \tag{A17} $$

[75] The equations are the same as for box 2, only the numerical subscripts on the right (the box index) must be changed.

A5. Sources and Sinks (SS)

[76]

$$ SS(\alpha)^{i}_{j} = -C^{i}_{Q,j} - \left(Q^{i}_{R,j} + Q^{i}_{L,j}\right) \cdot \alpha_{fw} \tag{A18} $$

$$ SS(\upsilon)^{i}_{j} = 0 \tag{A19} $$

$$ SS(\rho)^{i}_{j} = -\left(Q^{i}_{R,j} + Q^{i}_{L,j}\right) \cdot \rho_{air} + Q^{i}_{E,j} \cdot \rho^{i}_{\mathrm{sup},j} \tag{A20} $$

Appendix B: LSI Algorithm

[77] 1. If rank(**E**) < n (the number of unknowns) then stop the algorithm.

[78] 2. With the SVD of **E**, $\mathbf{E} = \mathbf{U}\cdot\mathbf{S}\cdot\mathbf{V}^{T}$, transform the original matrices **G**, **f** and **h**:

$$ \begin{aligned} \widetilde{\mathbf{G}} &= \mathbf{G}\cdot\mathbf{V}\cdot\mathbf{S}^{-1} \\ \mathbf{f}_1 &= \mathbf{U}^{T}\cdot\mathbf{f} \\ \widetilde{\mathbf{h}} &= \mathbf{h} - \mathbf{G}\cdot\mathbf{f}_1 \end{aligned} $$

[79] 3. Define the matrix (n + 1 × m) **A** and the vector (n + 1) **y:**

$$ \mathbf{A} = \begin{bmatrix} \widetilde{\mathbf{G}} \\ \widetilde{\mathbf{h}} \end{bmatrix}, \qquad \mathbf{y} = \begin{bmatrix} \overbrace{0\cdots 0}^{n} & 1 \end{bmatrix}^{T} $$

[80] 4. With the NNLS algorithm find the optimum (m vector) $\hat{\mathbf{u}}$ to the problem

$$ Min\left\{(\mathbf{A}\cdot\mathbf{u} - \mathbf{y})^{T}\cdot(\mathbf{A}\cdot\mathbf{u} - \mathbf{y})\right\} \text{subject to } \mathbf{u} \geq 0 $$

[81] 5. Calculate the (n + 1) column vector **r**:

$$ \mathbf{r} = \mathbf{A}\cdot\hat{\mathbf{u}} - \mathbf{y} $$

[82] 6. If $(\mathbf{r}^{T}\cdot\mathbf{r})^{1/2} = 0$ then the constraints are not compatible; stop the algorithm.

[83] 7. Calculate the n vector $\widetilde{\mathbf{z}}$:

$$ \widetilde{\mathbf{z}} = \left[-r_1/r_{n+1} \cdots -r_n/r_{n+1}\right]^{T} $$

[84] 8. Calculate the final optimum solution $\hat{\mathbf{x}}$ to the LSI problem:

$$ \hat{\mathbf{x}} = \mathbf{V}\cdot\mathbf{S}^{-1}\cdot(\widetilde{\mathbf{z}} + \mathbf{f}_1). $$

Notation

t	time (s).
T	temperature (°C).
S	salinity, PSS78 [*United Nations Educational, Scientific, and Cultural Organization*, 1987].
ρ	density (kg m^{-3}), EOS80 [*United Nations Educational, Scientific, and Cultural Organization*, 1987].
ρ_{fw}	density of fresh water, ρ ($S = 0$, $T = T_{air}$).
C_P	seawater specific heat at constant pressure (J kg^{-1} $°C^{-1}$) [*Fofonoff and Millard*, 1983].
C_P^{fw}	C_P of fresh water, C_P ($S = 0$, $T = T_{air}$).
$\alpha = \rho \cdot C_p \cdot T$	thermal energy content (J m^{-3}).
$\alpha_{fw} = \rho_{fw} \cdot C_P^{fw} \cdot T_{air}$	freshwater thermal energy content.
$\upsilon = \rho \cdot S$	salt content (m^{-3}).
A	area (m^2).
V	volume (m^3).
η	sea level (m).
Q	advective water flux (m^3 s^{-1}).
Q_E	evaporation (m^3 s^{-1}).
Q_L	rainfall (m^3 s^{-1}).
Q_R	river discharge or drainage (m^3 s^{-1}).
C_Q	net radiative flux (J s^{-1}).
M	exchange coefficient (m^3 s^{-1}).
Z_C	level of no motion (m).

Superscripts

U, B	upper (U) or bottom (B) semibox/semiwall of the actual box (numerical subscript on the right).
n, s	north or south semibox/semiwall of the actual box (numerical subscript on the right).

Right subscripts

x, y	applied to walls of the actual box (numerical subscript on the right), x refers to (semi)walls separating two different boxes and y refers to walls splitting a box in northern and southern semiboxes.
Z, Z_C, sup	applied in the horizontal surfaces of the actual box (numerical subscript on the right). Z is used with vertical fluxes (Q) and exchange coefficients (M). Z_C is used with tracers in the surface enclosed by Z_C. Also, sup refers to variables in the top surface of the box.
0, 1, 2, 3	four boxes, which are numbered from the head (San Simón Bay, box 0) to the mouth of the ria (box 3).

Left subscripts

1, 2	western (2) or eastern (1) semiwall of the actual box (numerical subscript on the right).

[85] **Acknowledgments.** The authors wish to thank the crew of the R/V *Mytilus*, C. Souto, and Gago and Victoria González for their excellent work and assistance in the CTD surveys, the IEO for the management of the Ons meteorological station, and E. Álvarez Fanjul (Ente Público Puertos del Estado) for the sea level time series. This work has been supported by FEUGA and CICYT (AMB 95 1084–CO3–03). During the writing of the manuscript, M.G.C. was supported by grants of MCYT (REN2002-02111/MAR), XUGA (PGIDT02 RMA C40203PR), and an "Isidro Parga Pondal" grant funded by the Xunta de Galicia. P.C.P. was supported by the I3P Ph.D. program (CSIC).

References

Allen, J. S. (1975), Coastal trapped waves in a stratified ocean, *J. Phys. Oceanogr.*, *5*, 300–325.

Allen, J. S., and R. L. Smith (1981), On the dynamics of wind-driven shelf currents, *Philos. Trans. R. Soc. London*, *302*, 617–634.

Allen, J. S., et al. (1983), Physical oceanography of continental shelves, *Rev. Geophys.*, *21*(5), 1149–1181.

Álvarez Fanjul, E., B. Pérez Gomez, and I. R. Sanchez-Arevalo (1997), A description of the tides in the eastern North Atlantic, *Prog. Oceanogr.*, *40*, 217–244.

Álvarez-Salgado, X. A., G. Rosón, F. F. Pérez, and Y. Pazos (1993), Hydrographic variability off the Rías Baixas (NW Spain) during the upwelling season, *J. Geophys. Res.*, *98*(C8), 14,447–14,455.

Álvarez-Salgado, X. A., J. Gago, B. M. Míguez, M. Gilcoto, and F. F. Pérez (2000), Surface waters of the NW Iberian margin: Upwelling on the shelf versus outwelling of upwelled waters from the Rías Baixas, *Estuarine Coastal Shelf Sci.*, *51*(6), 821–837.

Bakun, A. (1973), Coastal upwelling Indices, West Coast of North America, 1946–71, technical report, 12 pp, NOAA, Silver Spring, Md.

Bakun, A., and C. S. Nelson (1991), The seasonal cycle of wind-stress curl in subtropical eastern boundary current regions, *J. Phys. Oceanogr.*, *21*, 1815–1834.

Bevington, P. R., and D. K. Robinson (1992), *Data Reduction and Error Analysis for the Physical Sciences*, 2nd ed., 328 pp., McGraw-Hill, New York.

Charney, J. G. (1955), The generation of oceanic currents by wind, *J. Mar. Res.*, *14*(4), 477–498.

Csanady, G. T. (1984), Circulation induced by river inflow in well mixed water over a sloping continental shelf, *J. Phys. Oceanogr.*, *14*, 1703–1711.

Fiúza, A. F. G. (1983), Upwelling patterns off Portugal, in *Coastal Upwelling*, edited by E. Suess and J. Thiede, pp. 85–98, Springer, New York.

Fofonoff, N. P., and R. C. Millard Jr. (1983), Algorithms for computation of fundamental properties of seawater, *UNESCO Tech. Pap. Mar. Sci.*, *44*, 53 pp.

Fraga, F. (1981), Upwelling off the Galician coast, northwest Spain, in *Coastal Upwelling*, *Coastal Estuarine Sci.*, vol. 1, edited by F. A. Richards, pp. 176–182, AGU, Washington, D. C.

Frouin, R., A. F. G. Fiúza, I. Ambar, and T. J. Boyd (1990), Observations of a poleward surface current off the coasts of Portugal and Spain during winter, *J. Geophys. Res.*, *95*(C1), 679–691.

Garvine, R. W. (1985), A simple model of estuarine subtidal fluctuations forced by local and remote wind stress, *J. Geophys. Res.*, *90*(C6), 11,945–11,948.

Garvine, R. W. (1987), Estuary plumes and fronts in shelf waters: A layer model, *J. Phys. Oceanogr.*, *17*, 1877–1896.

Gay, P. S., J. O'Donnell, and C. A. Edwards (2004), Exchange between Long Island Sound and adjacent waters, *J. Geophys. Res.*, *109*, C06017, doi:10.1029/2004JC002319.

Geyer, W. R., J. H. Trowbridge, and M. M. Bowen (2000), The dynamics of a partially mixed estuary, *J. Phys. Oceanogr.*, *30*(8), 2035–2048.

Gilcoto, M., X. A. Álvarez Salgado, and F. F. Pérez (2001), Computing optimum estuarine residual fluxes with a multiparameter inverse model method (OERFIM): Application to the Ría de Vigo (NW Spain), *J. Geophys. Res.*, *106*(C12), 31,303–31,318.

Gill, A. E. (1982), *Atmosphere-Ocean Dynamics*, 1st ed., 662 pp., Elsevier, New York.

Godin, G. (1972), *The Analysis of Tides*, 264 pp., Liverpool Univ. Press, Liverpool, U. K.

Golub, G. H., and C. F. V. Loan (1996), *Matrix Computations*, 3rd ed., 664 pp., Johns Hopkins Univ. Press, Baltimore, Md.

Hansen, D. V., and M. Rattray (1965), Gravitational circulation in straits and estuaries, *J. Mar. Res.*, *23*, 104–122.

Haynes, R., and E. D. Barton (1990), A poleward flow along the Atlantic coast of the Iberian Peninsula, *J. Geophys. Res.*, *95*(C7), 11,425–11,441.

Haynes, R., and E. D. Barton (1991), Lagrangian observations in the Iberian coastal transition zone, *J. Geophys. Res.*, *96*(C8), 14,731–14,741.

Hickey, B. M., and N. S. Banas (2003), Oceanography of the U.S. Pacific Northwest coastal ocean and estuaries with application to coastal ecology, *Estuaries*, *26*(4B), 1010–1031.

Hickey, B. M., X. Zhang, and N. Banas (2002), Coupling between the California Current System and a coastal plain estuary in low riverflow conditions, *J. Geophys. Res.*, *107*(C10), 3166, doi:10.1029/1999JC000160.

Holloway, G. (1989), Subgridscale representation, in *Oceanic Circulation Models: Combining Data and Dynamics*, edited by D. L. T. Anderson and J. Willebrand, pp. 513–593, Springer, New York.

Inall, M. E., T. P. Rippeth, and T. J. Sherwin (2000), Impact of nonlinear waves on the dissipation of internal tidal energy at a shelf break, *J. Geophys. Res.*, *105*(C4), 8687–8705.

Janzen, C. D., and K.-C. Wong (2002), Wind-forced dynamics at the estuary-shelf interface of a large coastal plain estuary, *J. Geophys. Res.*, *107*(C10), 3138, doi:10.1029/2001JC000959.

Jay, D. A., and E. P. Flinchem (1997), Interaction of fluctuating river flow with a barotropic tide: A demonstration of wavelet tidal analysis methods, *J. Geophys. Res.*, *102*(C3), 5705–5720.

Jay, D. A., and E. P. Flinchem (1999), A comparison of methods for analysis of tidal records containing multi-scale non-tidal background energy, *Cont. Shelf Res.*, *19*(13), 1695–1732.

Jay, D. A., W. R. Geyer, R. J. Uncles, J. Vallino, J. Largier, and W. R. Boynton (1997), A review of recent developments in estuarine scalar flux estimation, *Estuaries*, *20*(2), 262–280.

Jeans, D. R. G., and T. J. Sherwin (2001), The variability of strongly nonlinear solitary internal waves observed during an upwelling season on the Portuguese shelf, *Cont. Shelf Res.*, *21*(16-17), 1855–1878.

Kasai, A., A. E. Hill, T. Fujiwaka, and J. H. Simpson (2000), Effect of the Earth's rotation on the circulation in regions of freshwater influence, *J. Geophys. Res.*, *105*(C07), 16,961–16,969.

Lawson, C. L., and R. J. Hanson (1995), *Solving Least Squares Problems*, 337 pp., Soc. for Ind. and Appl. Math., Philadelphia, Pa.

Maamaatuaiahutapu, K., V. Garçon, C. Provost, and H. Mercier (1998), Transports of the Brazil and Malvinas currents at their confluence, *J. Mar. Res.*, *56*, 417–438.

Mackas, D. L., K. L. Denman, and A. F. Bennett (1987), Least squares multiple tracer analysis of water mass composition, *J. Geophys. Res.*, *92*(C3), 2907–2918.

McClain, C. R., S.-Y. Chao, L. P. Atkinson, J. O. Blanton, and F. de Castillejo (1986), Wind-driven upwelling in the vicinity of Cape Finisterre, Spain, *J. Geophys. Res.*, *91*(C7), 8470–8486.

Míguez, B. M., L. Fariña-Busto, F. G. Figueiras, and F. F. Pérez (2001), Succession of phytoplankton assemblages in relation to estuarine hydrodynamics in the Ría de Vigo: A box model approach, *Sci. Mar.*, *65*(1), 65–76.

Monteiro, P. M. S., and J. L. Largier (1999), Thermal stratification in Saldanha Bay (South Africa) and subtidal, density-driven exchange with

the coastal waters of the Benguela upwelling system, *Estuarine Coastal Shelf. Sci.*, *49*, 877–890.
Mosby, H. (1936), Verdunstung und Strahlung auf dem Meere, *Ann. Hydrogr. Mar. Meteorol.*, *64*, 281–286.
Münchow, A., A. K. Masse, and R. W. Garvine (1992), Astronomical and nonlinear tidal currents in a coupled estuary shelf system, *Cont. Shelf Res.*, *12*(4), 471–498.
Officer, C. B. (1976), *Physical Oceanography of Estuaries (and Associated Coastal Waters)*, 465 pp., John Wiley, New York.
Officer, C. B. (1980), Box models revisited, in *Estuarine and Wetland Processes With Emphasis on Modelling*, edited by P. Hamilton and K. B. McDonald, pp. 65–114, Springer, New York.
Otto, L. (1975), *Oceanography of the Ría de Arosa (N. W. Spain)*, 210 pp., Koninklijk Ned. Meteorol. Inst., Staatsuitgeverij/'s-Gravenhage.
Pardo, P. C., M. Gilcoto, and F. F. Pérez (2001), Short-time scale coupling between termohaline and meteorological forcing in the Ría de Pontevedra, *Sci. Mar.*, *65, suppl. 1*, 229–240.
Pickard, G. L., and W. J. Emery (1990), *Descriptive Physical Oceanography: An Introduction*, 5th ed., 320 pp., Elsevier, New York.
Piedracoba, S., X. A. Álvarez-Salgado, G. Rosón, and J. L. Herrera (2005), Short-timescale thermohaline variability and residual circulation in the central segment of the coastal upwelling system of the Ría de Vigo (northwest Spain) during four contrasting periods, *J. Geophys. Res.*, *110*, C03018, doi:10.1029/2004JC002556.
Prego, R., and F. Fraga (1992), A simple model to calculate the residual flows in a Spanish Ría: Hydrographic consequences in the Ría of Vigo, *Estuarine Coastal Shelf. Sci.*, *34*, 603–615.
Prego, R., F. Fraga, and A. F. Ríos (1990), Water interchange between the Ría of Vigo and the coastal shelf, *Sci. Mar.*, *54*(1), 95–100.
Pritchard, D. W. (1956), The dynamic structure of a coastal plain estuary, *J. Mar. Res.*, *15*(1), 33–42.
Ríos, A. F., M. A. Nombela, F. F. Pérez, G. Rosón, and F. Fraga (1992a), Calculation of runoff to an estuary: Ría de Vigo, *Sci. Mar.*, *56*(1), 29–33.
Ríos, A. F., F. F. Pérez, and F. Fraga (1992b), Water masses in the upper and middle North Atlantic Ocean east of the Azores, *Deep Sea Res., Part II*, *39*(3/4), 645–658.
Rosón, G., X. A. Álvarez-Salgado, and F. F. Pérez (1997), A non-stationary box model to determine residual fluxes in a partially mixed estuary, based on both thermohaline properties: Application to the Ria de Arousa (NW Spain), *Estuarine Coastal Shelf. Sci.*, *44*(3), 249–262.
Sakov, P., and J. S. Parslow (2004), Optimisation technique for calculating water transport in a box model (Gippsland Lakes, Victoria, Australia), *Estuarine Coastal Shelf. Sci.*, *59*(3), 417–428.
Sea-Bird Electronics Inc. (2000), CTD data acquisition software. Seasoft 4.244 manual, 149 pp., Bellevue, Wash.
Sea-Bird Electronics Inc. (2003), SBE 25 Sealogger CTD, user's manual, 70 pp., Bellevue, Wash.
Simpson, J. H. (1997), Physical processes in the ROFI regime, *J. Mar. Syst.*, *12*(1–4), 311–323.
Smith, R. L. (1983), Circulation patterns in upwelling regimes, in *Coastal Upwelling*, edited by E. Suess and J. Thiede, pp. 13–35, Springer, New York.
Souto, C., M. Gilcoto, L. Fariña-Busto, and F. F. Pérez (2003), Modelling the residual circulation of a coastal embayment affected by wind driven upwelling: Circulation of the Ria de Vigo (NW Spain), *J. Geophys. Res.*, *108*(C11), 3340, doi:10.1029/2002JC001512.
Starr, V. P. (1968), *The Physics of Negative Viscosity Phenomena*, 256 pp., McGraw-Hill, New York.
Sverdrup, H. U. (1938), On the process of upwelling, *J. Mar. Res.*, *1*(2), 155–164.
Sverdrup, H. U., M. W. Johnson, and R. H. Fleming (1942), *The Oceans: Their Physics, Chemistry and General Biology*, 1087 pp., Prentice-Hall, Upper Saddle River, N. J.
Tarantola, A., and B. Valette (1982), Generalized nonlinear inverse problems solved using the least squares criterion, *Rev. Geophys.*, *20*(2), 219–232.
Torres, R., E. D. Barton, P. Miller, and E. Fanjul (2003), Spatial patterns of wind and sea surface temperature in the Galician upwelling region, *J. Geophys. Res.*, *108*(C4), 3130, doi:10.1029/2002JC001361.
Uncles, R. J. (2002), Estuarine physical processes research: Some recent studies and progress, *Estuarine Coastal Shelf Sci.*, *55*(6), 829–856.
United Nations Educational, Scientific, and Cultural Organization (1987), International oceanographic tables, *UNESCO Tech. Pap. Mar. Sci.*, *40*, 195.
Valle-Levinson, A. (1995), Observations of barotropic and baroclinic exchanges in the lower Chesapeake Bay, *Cont. Shelf Res.*, *15*(13), 1631–1647.
Valle-Levinson, A., L. P. Atkinson, D. Figueroa, and L. Castro (2003), Flow induced by upwelling winds in an equatorward facing bay: Gulf of Arauco, Chile, *J. Geophys. Res.*, *108*(C2), 3054, doi:10.1029/2001JC001272.
Wang, D.-P. (1979), Wind-driven circulation in the Chesapeake Bay, winter 1975, *J. Phys. Oceanogr.*, *9*, 564–572.
Weast, R. C. (Ed.) (1969), *CRC Handbook of Chemistry and Physics: A Ready-Reference Book of Chemical and Physical Data*, 49th ed., CRC Press, Boca Raton, Fla.
Weisberg, R. H., and L. Zheng (2003), How estuaries work: A Charlotte Harbor example, *J. Mar. Res.*, *61*(5), 635–657.
Wong, K.-C. (1994), On the nature of transverse variability in a coastal plain estuary, *J. Geophys. Res.*, *99*(C7), 14,209–14,222.
Wong, K.-C. (2002), On the wind-induced exchange between Indian River Bay, Delaware and the adjacent continental shelf, *Cont. Shelf Res.*, *22*(11-13), 1651–1668.
Wong, K.-C., and X. Lu (1994), Low-frequency variability in Delaware's inland bays, *J. Geophys. Res.*, *99*(C6), 12,683–12,695.
Wong, K.-C., and A. Münchow (1995), Buoyancy forced interaction between estuary and inner shelf: Observation, *Cont. Shelf Res.*, *15*(1), 59–88.
Wong, K.-C., and A. Valle-Levinson (2002), On the relative importance of the remote and local wind effects on the subtidal exchange at the entrance to the Chesapeake Bay, *J. Mar. Res.*, *60*(3), 477–498.
Wooster, W. S., A. Bakun, and D. R. McLain (1976), The seasonal upwelling cycle along the eastern boundary of the North Atlantic, *J. Mar. Res.*, *34*(2), 131–141.
Wunsch, C. (1996), *The Ocean Circulation Inverse Problem*, 442 pp., Cambridge Univ. Press, New York.
Yoshida, K. (1955), Coastal upwelling off the California coast, *Rec. Oceanogr. Works Jpn.*, *2*, 8–20.

X. A. Álvarez-Salgado, P. C. Pardo, and F. F. Pérez, Instituto de Investigaciones Marinas, CSIC, Eduardo Cabello 6, E-36208, Vigo, Spain.
M. Gilcoto, School of Chemistry, Physics, and Earth Sciences, Flinders University, GPO Box 2100, Adelaide, SA 5001, Australia. (miguel.gilcoto@flinders.edu.au)